

1 **Physiologic RNA Targets and Refined Sequence Specificity of Coronavirus EndoU**

2 Rachel Ancar¹, Yize Li², Eveline Kindler³ &⁴, Daphne A. Cooper⁵, Monica Ransom¹, Volker Thiel³
3 &⁴, Susan R. Weiss², Jay R. Hesselberth¹ and David J. Barton^{6*}

4 ¹ Department of Biochemistry and Molecular Genetics, Program in Molecular Biology, School of
5 Medicine, University of Colorado, Aurora, CO, United States.

6 ² Department of Microbiology, Perelman School of Medicine, University of Pennsylvania,
7 Philadelphia Pennsylvania, United States.

8 ³ Institute of Virology and Immunology IVI, Bern, Switzerland.

9 ⁴ Department of Infectious Diseases and Pathobiology, Vetsuisse Faculty, University of Bern,
10 Bern, Switzerland.

11 ⁵ Department of Immunology and Microbiology, School of Medicine, University of Colorado,
12 Aurora, CO, United States.

13 ⁶ Department of Immunology and Microbiology, Program in Molecular Biology, School of
14 Medicine, University of Colorado, Aurora, CO, United States.

15 * Corresponding Author

16 David J. Barton

17 E-mail: David.Barton@CUAnschutz.edu

18 **ABSTRACT**

19 Coronavirus EndoU inhibits dsRNA-activated antiviral responses; however, the physiologic RNA
20 substrates of EndoU are unknown. In this study, we used mouse hepatitis virus (MHV)-infected
21 bone-marrow-derived macrophage (BMM) and cyclic phosphate cDNA sequencing to identify
22 the RNA targets of EndoU. EndoU targeted viral RNA, cleaving the 3' side of pyrimidines with a
23 strong preference for U[↓]A and C[↓]A sequences (endoY[↓]A). EndoU-dependent cleavage was
24 detected in every region of MHV RNA, from the 5' NTR to the 3' NTR, including transcriptional
25 regulatory sequences (TRS). Cleavage at two CA dinucleotides immediately adjacent to the
26 MHV poly(A) tail suggest a mechanism to suppress negative-strand RNA synthesis and the
27 accumulation of viral dsRNA. MHV with EndoU (EndoU^{mut}) or 2'-5' phosphodiesterase (PDE^{mut})
28 mutations provoked the activation of RNase L in BMM, with corresponding cleavage of RNAs by
29 RNase L. The physiologic targets of EndoU are viral RNA templates required for negative-
30 strand RNA synthesis and dsRNA accumulation.

31 **Impact:** Coronavirus EndoU cleaves U[↓]A and C[↓]A sequences (endoY[↓]A) within viral (+) strand
32 RNA to evade dsRNA-activated host responses.

33 INTRODUCTION

34 Viruses in the order *Nidovirales* express a virus-encoded endoribonuclease, NendoU (1).
35 NendoU is unique to nidoviruses (2), including viruses of the *Coronaviridae* and *Arteriviridae*
36 families. Nidoviruses that express NendoU have vertebrate hosts whereas nidoviruses of
37 crustaceans (*Roniviridae*), and RNA viruses outside the *Nidovirales* order, do not encode this
38 protein. The precise role(s) of NendoU in virus replication remain enigmatic; however, significant
39 progress has been made in recent years to elucidate the contributions of NendoU to virus
40 replication and pathogenesis. The SARS-CoV-2 pandemic underscores the importance of
41 understanding host-pathogen interactions, including the immunomodulatory functions of EndoU
42 (3).

43 Arterivirus (nsp11) and coronavirus (nsp15) EndoU proteins have been characterized by
44 genomic (2), structural (4-6) and biochemical studies (6-8). EndoU is encoded near the 3' end of
45 ORF1b (Fig. 1A, schematic of MHV genome) (2). Mouse hepatitis virus (MHV), a well-studied
46 coronavirus, has a single-stranded positive-sense RNA genome 31.1 kb in length. MHV RNA,
47 like other coronaviruses, is 5' capped and 3' polyadenylated. Upon infection, the ORF1a and
48 ORF1b regions of MHV RNA are translated into two polyproteins (ORF1a and ORF1ab) through
49 a frame shifting mechanism (9). MHV proteins nsp1-nsp16 are produced via proteolytic
50 processing of the ORF1a and ORF1ab polyproteins. EndoU is the nsp15 protein of MHV (Fig.
51 1A, schematic of MHV RNA genome). Other proteins from the ORF1a/1b region of the RNA
52 genome include viral proteases and components of the viral replicase (nsp12 is the RdRP,
53 nsp13 is a helicase, nsp14 is a 3'→5' exonuclease and a N7-methyl transferase, and nsp16 is a
54 2'-O-methyl transferase). An H277A mutation in nsp15 disables the catalytic activity of EndoU
55 (Fig. 1A, EndoU^{mut}).

56 Coronavirus RNA replication and RNA transcription are mediated by the replicase expressed
57 from the ORF1a/1b region of the genome, with assistance of the nucleocapsid protein (10). Both

58 RNA replication and RNA transcription occur within membrane-anchored replication organelles
59 in the cytoplasm of infected cells (11-13). MHV RNA replication involves negative-strand RNA
60 synthesis, wherein the positive-strand viral RNA genome is copied into a genome-length
61 negative-strand RNA intermediate, which is subsequently used as a template to make new
62 positive-strand RNA genomes. MHV RNA transcription involves the synthesis of subgenomic
63 (sg) negative-strand RNAs from the viral RNA genome via discontinuous transcription
64 mechanisms and subsequent synthesis of sg mRNAs (14, 15). Intergenic transcriptional
65 regulatory sequences (TRS) within MHV RNA guide discontinuous transcription mechanisms
66 (16), leading to the production of sg negative-strand RNAs, which function as templates for the
67 synthesis of sg mRNAs. A nested set of 3' co-terminal sg mRNAs (sg mRNA2 to sg mRNA7) is
68 used to express each of the remaining viral proteins [phosphodiesterase (PDE) from sg
69 mRNA2a; spike (S) from sg mRNA3, and so forth). Hemagglutinin-esterase (HE) is an
70 unexpressed pseudogene in MHV A59 due to a TRS mutation that prevents the expression of
71 mRNA2b, as well as a nonsense mutation at codon 15 (17-20). EndoU co-localizes with viral
72 RNA replication and RNA transcription machinery at membrane-anchored replication organelles
73 (21, 22). Co-localization of EndoU with viral RNA synthesis machinery may influence the RNAs
74 targeted by EndoU. Furthermore, coronavirus nsp16, a 2'-O-ribose-methyltransferase (2'-O'MT),
75 could potentially modify RNA substrates to make them resistant to cleavage by EndoU (1).
76 These studies suggest that viral RNA stability may be regulated by nsp15 (EndoU) and nsp16
77 (2'-O'MT).
78 Intriguingly, neither EndoU (nsp15) nor 2'-O'MT (nsp16) enzyme activities are required for virus
79 replication in transformed cells in culture (23-25); rather, these enzymes counteract dsRNA-
80 activated antiviral responses (22, 25, 26). EndoU catalytic activity prevents the activation of
81 dsRNA-dependent antiviral innate immune pathways (22, 26), including Type I and Type III IFN
82 responses, PKR and OAS-RNase L (27). EndoU-deficient viruses can replicate in IFNAR^{-/-} cells

83 or cells lacking PKR and RNase L (PKR^{-/-} & RNase L^{-/-}) (22, 26, 27). In addition to EndoU,
84 coronavirus NS2, a 2'-5' PDE, prevents activation of RNase L (28-30). Thus, there are two
85 pathways by which MHV prevents activation of OAS-RNase L suggesting this pathway is crucial
86 for antiviral defense. While coronavirus EndoU inhibits dsRNA-activated antiviral responses
87 within virus-infected cells, it is unclear how it achieves this because the physiologically relevant
88 targets of EndoU have not been defined.

89 In this study, we used MHV-infected bone marrow-derived macrophage (BMM) and cyclic
90 phosphate cDNA sequencing to identify the host and viral RNA targets of EndoU. Cyclic
91 phosphate cDNA sequencing reveals the location and frequency of endoribonuclease cleavage
92 sites within host and viral RNAs (31-34). We exploited wildtype and mutant forms of MHV (wt
93 MHV, PDE^{mut}, and EndoU^{mut}) along with wildtype and mutant forms of BMM (wt BMM, IFNAR^{-/-}
94 and RNase L^{-/-}) to distinguish between EndoU-dependent cleavage sites and RNase L-
95 dependent cleavage sites within host and viral RNAs.

96 **MATERIALS AND METHODS**

97 **Viruses**

98 Wildtype Mouse Hepatitis Virus A59 from Volker Thiel [MHV^(V)] (35-37) and Susan Weiss
99 [MHV^(S)] (38) were used, along with a mutant derivative of each. An H277A mutation in nsp15
100 rendered an EndoU-deficient mutant (EndoU^{mut}) from MHV^(V) (26). An H126R mutation in NS2
101 rendered a phosphodiesterase mutant (PDE^{mut}) from MHV^(S) (38).

102 **Murine bone marrow-derived macrophages**

103 Bone marrow-derived macrophage (BMM) from WT, IFNAR^{-/-} and RNase L^{-/-} C57BL/6 mice
104 were obtained as previously described (26). Progenitor cells were isolated from the hind limbs of
105 8-12 week old mice, passed through a cell strainer and RBCs were lysed using 1 ml of lysis
106 buffer (0.15 M NH₄Cl, 1 mM KHCO₃, 0.1 mM EDTA). Cells were washed 3x with PBS and
107 cultured in macrophage medium (Iscove's Modified Dulbecco's Medium, 5-10% M-CSF (L929-
108 supernatant), 0.1% 50 mM 2-mercaptoethanol). Adherent BMM were harvested at 7 dpi.

109 **Virus infection**

110 BMM were infected with MHV^(S), MHV^(V), EndoU^{mut}, and PDE^{mut} at an MOI of 1 PFU per cell at
111 37°C as previously described (26). At 9 and 12 hours post-infection (hpi), supernatant was
112 harvested for virus titration and cells were lysed in Trizol (Invitrogen). MHV in the supernatant
113 was quantified by standard plaque assay on L2 cells.

114 **Cyclic phosphate cDNA sequencing**

115 Total RNA was extracted from cell lysates and split equally for cyclic phosphate and RNAseq
116 library preparations. Cyclic phosphate cDNA libraries were prepared by DNase treating the total
117 RNA for 30 min followed by ethanol precipitation with 20 μg of glycogen and ligation with 50 μM
118 3'-linker in 30 μl final volume. The ligation reactions were conducted using 15 pmol of RtcB

119 ligase (NEB), 1x RtcB buffer (NEB), 100 μM GTP, 1 mM MnCl₂, 20 units of RNase inhibitor
120 (Enzymatics) at 37°C for 2 h. Samples were ethanol precipitated with 20 μg of glycogen and
121 resuspended in 10 μl of RNase free H₂O for chemical fragmentation (Ambion Fragmentation
122 Reagent) at 65°C for 4 min. Samples were then denatured in 1 volume of stop dye (95%
123 formamide, 0.01% xylene cyanol / bromophenol blue), heated to 65°C for 5 min and separated
124 on a 6 % polyacrylamide TBE–urea gel. Gels were stained with SYBR Gold (Invitrogen) and
125 visualized to excise RNA larger than adapter (~100-1000 bp). RNA was eluted from the gel
126 slices with 2 h incubation at 40°C in 0.3 M sodium acetate, pH 5.2, 1 mM EDTA, pH 8.0 followed
127 by gentle mixing overnight at 4°C. Eluted RNA was recovered by ethanol precipitation with 20
128 μg of glycogen and resuspended in 12 μl of RNase free H₂O. RNA was ligated to 50 μM 5'-
129 linker in 20 μl final volume. The ligation reactions were conducted using 15 pmol of RtcB (NEB),
130 1x RtcB buffer (NEB), 100 μM GTP, 1 mM MnCl₂, 20 units of RNase inhibitor (Enzymatics) at
131 37°C for 2 h followed by ethanol precipitation with 20 μg of glycogen and resuspended in 100 μl
132 of RNase free H₂O. Ligated RNAs were purified using 25 μl of magnetic Streptavidin beads
133 (Invitrogen) washed three times with 100 μl of B&W buffer [5 mM Tris-HCl (pH 7.5), 0.5 mM
134 EDTA, 1 M NaCl] supplemented with 0.1% Tween 20, twice with 100 μl of solution A (0.1 M
135 RNase free NaOH, 0.05 M RNase free NaCl), and twice with 100 μl of solution B (0.1 M RNase
136 free NaCl). Washed beads were resuspended in 2x B&W buffer [10 mM Tris-HCl (pH 7.5), 1
137 mM EDTA, 2 M NaCl], with 20 units of RNase inhibitor (Enzymatics) and the RNA solution was
138 added to the beads and incubated with rotation for 15 min at room temperature. After incubation,
139 the beads were washed three times with 100 μl of 1x B&W buffer before resuspending the
140 beads in 20 μl of 25 mM biotin in elution buffer (Omega BioTek). The beads were incubated at
141 room temperature for 15 min with occasional mixing. After binding the beads to the magnet, the
142 supernatant was collected. The elution process was repeated once for a final volume for 40 μl of

143 eluted RNA. cDNA was prepared using 5 μM of an Illumina-compatible primer complimentary to
144 the 3'-linker, 20 ul of eluted RNA, and Protoscript II RT (NEB). 10 μl of cDNA was PCR
145 amplified for 18 cycles with Illumina TruSeq primers and Phusion DNA polymerase. PCR
146 reactions were purified with AMPure XP beads (Beckman Coulter). Indexed libraries were
147 quantified by Qubit (Invitrogen). Library quality was assessed on a 4200 TapeStation System
148 Instrument (Agilent Technologies) using a D100 ScreenTape assay, mixed to a final
149 concentration of 1–10 nM and sequenced on an Illumina HiSeq in a 50 cycle run.

Oligonucleotides	Sequences
3p-RNA linker (RNA oligo)	5' rNrNrNrNrNrNrNrNrArGrArUrCrGrGrArArGrArGrCrGrUrCrGrUrG/3'-desBIOTeg/
5p-RNA linker (RNA oligo)	/5' AmMC6/rGrUrGrArCrUrGrGrArGrUrUrCrArGrArCrGrUrGrUrGrCrUrCrUrUrCrCrGr rArUrC/3'-Phos/
ILMN-RT	5'-ACACGACGCTCTTCCGATCT-3'
TruSeq Universal PCR Forward	5' AATGATACGGCGACCACCGAGATCTACACTCTTTCCCTACACGACGCTCTTCCGATCT-3'
TruSeq Indexed PCR Reverse	5' CAAGCAGAAGACGGCATAACGAGATCGGTNNNNNNGTGACTGGAGTTTCAGACGTGTGCTCTTCCGAT-3'

150 **Stranded RNAseq**

151 Total RNA was enriched for polyadenylated mRNA using oligo-dT magnetic beads (Ambion).
152 cDNA was generated from the enriched polyA⁺ mRNAs after fragmentation in 2.2x SuperScript
153 IV reverse transcriptase buffer at 94°C for 3 min. After immediately cooling on ice, RT reaction
154 with SuperScript IV RT (Thermo Fisher Scientific) was performed per manufacture's
155 recommendations with 150 ng of random primers (Thermo Fisher Scientific) in 20 μl final
156 volume. cDNA:RNA hybrids were purified using MyOne Silane beads (Thermo Fischer
157 Scientific) per manufacture's recommendations and eluted in 18 μl of RNase free H₂O. Second-
158 strand cDNA was then generated using RNase H and *E. coli* DNA Polymerase (Enzymatics)
159 with dUTP incorporation (1x NEB buffer 2, 100 μM dATP, dCTP, dGTP, 200 μM dUTP, 2.5 units
160 of RNase H, 30 units of DNA polymerase) in 100 μl final volume at 15°C for 2.5 hrs. cDNA was

161 purified with Silane beads and eluted in 52 μ l of RNase free H₂O as input for end repair reaction
162 using End Repair Module (NEB) following manufacturer's recommendations. A-tailing reaction
163 (50 μ l final volume) performed with Klenow fragment (minus 3'-5' exonuclease activity,
164 Enzymatics) and end repaired Silane purified cDNA eluted in in 32 μ l of RNase free H₂O (1x
165 NEB buffer 2, 200 μ M dATP, 15 units Klenow fragment) at 37°C for 30 min. Reaction products
166 were purified with 1.8x AMPure XP beads (Beckman Coulter) and eluted in 10 μ l of RNase free
167 H₂O. Purified cDNA was ligated to 40 nM of annealed Illumina TruSeq Universal adaptors in 50
168 μ l final volume reaction for 30 min at 25°C (40 nM adaptors, 1X Rapid Ligation Buffer
169 (Enzymatics), 3000 units of T4 DNA ligase (Enzymatics). Reaction products were purified with
170 AMPure XP beads and eluted in 12 μ l of RNase free H₂O. USER enzyme (NEB) was used to
171 degrade the dUTP-containing strand by adding 1 unit of USER to purified cDNA and incubating
172 for 30 min at 37°C. Reactions were used directly in PCR amplification with Illumina TruSeq
173 primers and Phusion DNA polymerase with 10 μ l of input for 18 cycles. Libraries were size
174 selected from 200 – 700 bp using AMPure XP beads, quantified by Qubit (Invitrogen), and
175 mixed to a final concentration of 4 nM. Library quality was assessed on a 4200 TapeStation
176 System Instrument (Agilent Technologies) using a D100 ScreenTape assay and sequenced on
177 an Illumina NovaSEQ 6000 in a paired end 150 cycle run.

Adaptors	Sequences
Illumina forward (F)	/5' -Phos/GATCGGAAGAGCTCGTATGCCGTCTTCTGCTTG-3'
Illumina reverse (R)	/5' - ACACTCTTTCCCTACACGACGCTCTTCCGATC*T-3'

178 **Computational analyses of next generation sequencing data**

179 *Processing and analysis of cyclic phosphate cDNA libraries*

180 Unique molecular identifier (UMI) sequences were extracted and added to FASTQ reads using
181 UMI-tools (v0.5.4) (39). Only read 1 was used from the second experiment, to adhere with the

182 analysis process applied for experiment 1. FASTQ reads were then aligned to the MHV genome
183 alone (GenBank accession: NC_001846.1) and a combined reference including the MHV
184 genome, *Mus musculus* rRNA and U6 snRNA references (GenBank accession numbers:
185 NR_003278.3, NR_003279.1, NR_003280.2, NC_000074.6, NR_003027.2), and annotated
186 ORFs from the Mouse ORFeome collection (MGC full-cds collection for *Mus musculus*)
187 using Bowtie version 2 (v2.3.2) (40). Aligned reads were de-duplicated using UMI-tools to
188 remove PCR duplicated reads. De-duplicated reads were converted to bedGraph format using
189 BEDTools (v2.26.0) to report the number of reads at each single base cleavage position,
190 including for sense and antisense sequences for the MHV aligned reads (41). Reads at each
191 cleavage position were normalized by library size.

192 To identify signal dependent on the presence of a specific endoribonuclease, normalized counts
193 at each cleavage position in RNase L^{-/-} or EndoU^{mut} libraries were subtracted from the signal in
194 libraries with wild type RNase L or EndoU activity, to remove signal that occurred in the absence
195 of either endoribonuclease. The difference in cleavage activity at each position in the absence
196 of RNase L or EndoU was determined by calculating the log₂ fold change. The frequency of
197 cleavage at particular dinucleotides was determined by quantifying the sum of reads assigned to
198 each of the 16 possible dinucleotides divided by total number of aligned reads in the library.
199 Dinucleotide enrichment was determined by calculating the frequency of cleavage at each
200 dinucleotide in the MHV genomic sequence and determining the log₂ fold enrichment of the
201 observed (experimental) frequencies compared to the expected (background) frequencies.
202 Significance of enrichment was calculated using the Fisher's exact test to compare the odds
203 ratio of obtaining a specific dinucleotide in the expected data to the observed data.

204 *RNAseq alignment, annotation, and differential expression analysis*

205 Illumina adaptor sequences were trimmed from FASTQ reads using Cutadapt (v 1.16) and
206 sequences shorter than 20 nucleotides were discarded (42). Trimmed reads were aligned to a

207 combined MHV (GenBank accession: NC_001846.1) and *Mus musculus* genome reference
208 (Ensemble GRCm38.p6) and bedGraph coverage files were generated from each alignment
209 using STAR (v 2.7.1a) (43). Read fragments were assigned and counted using featureCounts
210 (from subread v 1.6.2) and a combined MHV and *Mus musculus* GTF (Ensemble GRCm38.p6)
211 file for gene annotation (44). The MHV GTF file included the genomic positions of the combined
212 ORF1a/b non-structural proteins and each of the structural and accessory proteins. Gene
213 counts were normalized using DESeq2 media of ratios method to account for sequencing depth
214 and RNA composition (45). For downstream differential expression analysis, trimmed reads
215 were also aligned to the *Mus musculus* complete transcriptome reference (Gencode
216 GRCm38.p6) using Salmon (v.0.14.1) (46). Transcript abundance files were used for differential
217 expression analysis with DESeq2 after importing with tximport and counts normalized by the
218 media of ratios method were used for data visualization (47). Genes with an FDR < 0.05 were
219 called significant and used to generate volcano plots with the EnhancedVolcano package and z-
220 transformed counts were used to generate heatmaps with the ComplexHeatmap package (48,
221 49). For gene functional category enrichment analyses, topGO was used to determine
222 significant enrichment (weightFish/p > 0.01) by using non-differentially expressed genes (< 2 or
223 < -2 log₂ fold change and FDR < 0.01) as the background to determine the categories enriched
224 in differentially expressed genes. topGO employs conditional enrichment analysis, which takes
225 the nested structure of GO terms into account to reduce redundancy in enrichment results (50).

226 *Motif analysis*

227 To visualize the cleavage sequence preferences for RNase L and EndoU, the top 1% of
228 either RNase L- or EndoU-dependent sites from subtractive analysis, as described above, were
229 selected. Using BEDTools, 3 bps were added upstream and downstream of the selected
230 positions and a FASTA file was generated from the 6-base pair sequences. Meme was used to
231 determine the sequence preference enrichment and graphed using ggseqlogo (51, 52).

232 *UA scoring*

233 UA sequences in the MHV genome were designated as predominantly cleaved 3' of U
234 (consistent with EndoU targeting) or A (consistent with RNase L targeting). All UA dinucleotides
235 in the MHV genome with > 30 cyclic phosphate counts at either position of cleavage in the
236 dinucleotide were selected and the ratio of normalized counts in each position was calculated
237 (RNase L / EndoU). If the ratio was > 1, the position was scored as a UA[↓] site and if the ratio
238 was < 1 the position was scored as a U[↓]A.

239 *Regional MHV cleavage analysis and abundance normalization*

240 The normalized counts in each MHV genomic region (all the genes and ORFs shown in Figure
241 1A, in addition to the 5' and 3'-UTR and body TRS regions) were summed to calculate the total
242 cyclic phosphate reads per region. Size correction was performed by dividing the sum of cyclic
243 phosphate counts in each region by the length of the region in bases. To normalize the cyclic
244 phosphate data by RNA abundance, stranded bedGraph files were generated from the bam files
245 produced by STAR alignment of the RNAseq libraries. At each position with both cyclic
246 phosphate and RNAseq data in the MHV genome, the cyclic phosphate counts were divided by
247 the normalized (reads per million mapped reads) RNAseq counts to generate an abundance
248 normalized cyclic phosphate value.

249 *TRS analysis*

250 In the above analyses, RNAseq reads mapping to the viral genome were not distinguished by
251 alignment to genomic RNA or subgenomic mRNAs. To assign RNAseq reads to subgenomic
252 mRNAs, we employed an analysis similar to that described in Irigoyen et al., 2016 (53) to
253 identify leader/body chimeric reads (subgenomic mRNAs). We parsed the bam files generated
254 from STAR alignment of the RNAseq libraries to the combined mouse and MHV genome for
255 reads containing the 11 nucleotides of the leader sequence, UUUAAAUCUAA (GenBank
256 accession: NC_001846.1, nt 54 – 65) before the leader TRS sequence. The positions in the

257 reference where the read alignment starts and ends after the leader sequence were extracted to
258 obtain an interval of alignment for the sequence downstream of the leader/body transition. The
259 intervals for each chimeric read were intersected with the intervals of each canonical
260 subgenomic mRNA using valr (54), with the requirement of at least 30 nt of overlap, to assign
261 each chimeric read to an mRNA: 65 to 21746 (mRNA 1), 21747 to 23921 (mRNA 2), 23922 to
262 27934 (mRNA 3), 27935 to 28317 (mRNA 4), 28318 to 28959 (mRNA 5), 28958 to 29654
263 (mRNA 6), 29655 to 31334 (mRNA 7) (54). The number of reads assigned to each mRNA were
264 counted and normalized to either the total sum of mRNAs per library or reads per million.

265 *SNP analysis*

266 Variant calling analysis was performed using bcftools (v1.9) to generate genotype likelihoods
267 from the RNAseq bam files for MHV aligned reads, followed by SNP calling/indel calling to
268 generate VCF files (55). The generated VCF files were filtered using bcftools with parameters -s
269 LOWQUAL -e %QUAL<30 || DP>20' to identify low quality sites with less than 20 quality score
270 or 30 base pairs of read depth.

271 **Data Deposition**

272 Raw and processed sequencing data are available at NCBI GEO: GSE147852.

273 **Bioinformatics Pipeline**

274 Code for all described analyses are available at <https://github.com/hesselberthlab/endoU> in the
275 form of scripts, a data processing pipeline, and analysis package.

276 RESULTS

277 Products of cleavage by coronavirus EndoU have 2',3'-cyclic phosphate termini (1), effectively
278 marking the location of cleavage within host and viral RNAs. Thus, in this study, we used cyclic
279 phosphate cDNA sequencing to monitor the frequency and location of endoribonuclease
280 cleavage sites in RNA from MHV-infected bone marrow-derived macrophage (BMM) (Fig. 1).
281 Wildtype and mutant MHVs [wt MHV^(V), wt MHV^(S), PDE^{mut}, and EndoU^{mut}] along with BMM
282 derived from wildtype and particular knockout C57BL/6 mice [WT, IFNAR^{-/-} and RNase L^{-/-} BMM]
283 were used to distinguish between EndoU-dependent cleavage sites and RNase L-dependent
284 cleavage sites (Fig. 1B). A pair of wt and mutant viruses derived from each isolate were used
285 (Figs. 1A and 1B): wt MHV from Susan Weiss' lab designated MHV^(S) and a phosphodiesterase
286 mutant designated PDE^{mut} (28-30, 38); wt MHV from Volker Thiel's lab designated MHV^(V) and
287 an EndoU mutant designated EndoU^{mut} (26). Total cellular RNA was isolated from cells at 9 and
288 12 hpi, times when coronavirus NS2 PDE and nsp15 EndoU activities prevent dsRNA-
289 dependent antiviral responses (26), including the OAS/RNase L pathway (28-30). Under these
290 experimental conditions (Fig. 1B), we expect that RNase L activity will be increased within
291 PDE^{mut}-infected and EndoU^{mut}-infected WT BMM, as compared to MHV^(S)-infected and MHV^(V)-
292 infected WT BMM. Furthermore, we expect that EndoU activity will be evident within MHV^(S)-
293 infected and MHV^(V)-infected BMM, as compared to EndoU^{mut}-infected BMM.

294 Cyclic phosphate cDNA libraries were prepared using total cellular RNA from 9 and 12 hpi (Fig.
295 1C). The RNA ligase RtcB was used to ligate a 3' adaptor to RNA fragments containing a cyclic
296 phosphate. The 3' adaptor has a biotin moiety and a unique molecular identifier to enumerate
297 cleavage sites (56). A 5' adaptor was ligated to the RNA samples, followed by reverse
298 transcription, PCR amplification and Illumina sequencing. Analysis of DNA sequences revealed
299 the frequency and location of endoribonuclease cleavage sites in host and viral RNAs. Figures
300 2-8 in the body of this manuscript correspond to data from the experiment outlined here (Fig. 1).

301 Replicate data from infections by wt and mutant MHV [wt MHV^(S), PDE^{mut}, and EndoU^{mut}] in wt
302 and RNase L^{-/-} BMM yield similar outcomes (Figures S8 and S9).

303 **Endoribonuclease cleavage sites in host and viral RNAs.** Endoribonuclease cleavage sites
304 were detected in both host and viral RNAs (Fig. 2). The frequency of cleavage sites in individual
305 RNAs was normalized to percent total cDNA reads in each library, allowing for quantitative
306 comparisons between individual RNAs in each sample and between RNAs across distinct
307 samples. The vast majority of cleavage sites were detected in MHV RNA, cellular mRNA and
308 ribosomal RNAs (18S, 28S 5.8S and 5S rRNAs), with a smaller portion of cleavage sites in
309 tRNAs and U6 snRNA (Fig. 2). We can attribute cleavage sites in cellular RNAs to specific
310 endoribonucleases in some cases, but not others. For instance, U6 snRNA had 3'-terminal
311 cyclic phosphates (Fig. S1A) attributed to the nucleolytic activity of C16orf57/USB1 (32, 57, 58).
312 Ribosomal RNAs accounted for ~50-80% of the cleavage sites detected in each library (Fig. 2).
313 The majority of cleavage sites within rRNAs are the result of unspecified endoribonucleases,
314 along with some RNase L-dependent cleavage sites (31, 32), as described below. Cellular
315 mRNAs accounted for ~5% of endoribonuclease cleavage sites in each cDNA library (Fig. 2);
316 however, the numbers of cleavage sites within individual cellular mRNAs were too low to
317 definitively attribute to one or another endoribonuclease.

318 Cleavage sites in MHV RNA were found predominantly in the positive-strand of viral RNA,
319 ranging from 10% to 40% of all cleavage sites in each library (Fig. 2). Very few reads were
320 detected in the MHV negative-strand RNA (Fig. S1B, S11C-D). As described below, we attribute
321 cleavage sites in MHV RNA to specific endoribonucleases, including EndoU and RNase L.

322 In WT BMM, we captured more reads per library mapping to MHV RNA at 12 hpi as compared
323 to 9 hpi, except in cells infected with EndoU^{mut} MHV. However, in IFNAR^{-/-} and RNase L^{-/-} BMM,
324 capture of MHV RNA was similar between 9 and 12 hpi (Fig 2). Across all cell types the relative
325 amount of host RNAs captured at 9 and 12 hpi were similar and in agreement with capture

326 frequencies from uninfected and virus-infected cells previously reported (25, 26, 46). Data from
327 an independent experiment revealed similar outcomes, with 10% to 30% of all cleavage sites in
328 MHV RNA, 5% to 10% of cleavage sites in cellular mRNA and more than 60% of cleavage sites
329 in ribosomal RNAs (Fig. S8A).

330 **Frequency, location and sequence specificity of cleavage sites in MHV RNA.** Metal-ion-
331 independent endoribonucleases have characteristic specificities: e.g. RNase A family members
332 (RNase 1-8) cleave RNA 3' of pyrimidines while RNase L cleaves RNA 3' of UpN[↓] dinucleotides
333 (UA[↓], UU[↓] > UG[↓]) (32, 59). EndoU is reported to cleave RNA 3' of pyrimidines in vitro (1, 8, 60);
334 however, physiologically relevant targets of EndoU have not been defined.

335 We detected endoribonuclease cleavage sites throughout MHV RNA, under all experimental
336 conditions (Fig. 3). The frequency of cleavage at each base of MHV RNA ranged from ~ 0.00 to
337 0.2% of all cDNA reads in each library (Fig. 3, y-axis). Peaks of cleavage approaching 0.2% of
338 all cDNA reads in each library (corresponding to 1 in 500 cleavage sites across all RNAs in
339 each cDNA library) are present at particular sites in the N gene open reading frame, near the 3'
340 terminus of MHV RNA (Fig. 3, WT BMM, PDE^{mut} and EndoU^{mut}). Typically, when measurable
341 cleavage was detected at a particular base in MHV RNA at 9 hpi, measurable cleavage was
342 also detected at that same site at 12 hpi, often with increased abundance (Fig. 3, overlapping
343 orange and blue lines at each base for 9 and 12 hpi).

344 The sequence specificity of cleavage sites in MHV RNA revealed profound differences in the
345 endoribonuclease activities present within WT BMM cells infected with WT and mutant viruses
346 (Fig. 4). Distinct RNase L-dependent and EndoU-dependent cleavage specificities were evident
347 (Fig. 4). The sequence specificity of endoribonuclease cleavage sites was assessed in two
348 registers: positions -2 to -1 of cleavage (Fig. 4A, B and C) and positions -1 to +1 of cleavage
349 (Fig. 4D, E and F). WT MHV RNA was cleaved 3' of pyrimidines in WT BMM [Fig. 4A, MHV^(S)
350 and MHV^(V)], with a notable preference for cleavage between U[↓]A and C[↓]A sequences (Fig. 4D,

351 E and F). This pattern of pyrimidine specific cleavage between U \downarrow A and C \downarrow A sequences was
352 lost in Endo^{mut}-infected WT BMM (Fig. 4A and 4D). Similar patterns of cleavage were evident in
353 an independent experiment (Fig. S8C-D).

354 Dinucleotide enrichment, a measurement comparing the frequency of cleavage at each
355 dinucleotide to the frequency of each dinucleotide in the MHV genomic RNA, showed that U \downarrow A
356 and C \downarrow A sequences were the only sequences with positively enriched cleavage in WT MHV-
357 infected WT BMM (Fig. 4E, adjusted p-value (q) for fold change [$\log_2(\text{experiment} / \text{control})$] of
358 $<1 \times 10^{8***}$). Dinucleotide enrichment and de-enrichment data for all dinucleotides at 9 and 12 hpi
359 are available as supplemental data (Tables S1 and S2). These data indicate that EndoU
360 cleaved MHV RNA at U \downarrow A and C \downarrow A sequences.

361 RNase L activity was also evident within MHV-infected WT BMM (Fig. 4A, B and C). RNase L
362 activity, with characteristic cleavage predominantly after UA \downarrow and UU \downarrow dinucleotides, was
363 significantly increased in both PDE^{mut}-infected and EndoU^{mut}-infected WT BMM (Fig. 4A).
364 Dinucleotide enrichment showed that UA \downarrow , UU \downarrow and UC \downarrow sequences were positively enriched
365 cleavage sites in PDE^{mut}-infected and EndoU^{mut}-infected WT BMM (Fig. 4B, adjusted p-value (q)
366 for fold change [$\log_2(\text{experiment} / \text{control})$] of $<1 \times 10^{8***}$). In IFNAR^{-/-} and RNase L^{-/-} BMM, the
367 robust cleavage at UA \downarrow , UU \downarrow and UC \downarrow sequences decreased and pyrimidine specific cleavage
368 dominated, especially in PDE^{mut}-infected cells (Figs. S3A and S3B). These data indicate that
369 RNase L cleaved MHV RNA after UA \downarrow , UU \downarrow and UC \downarrow sequences, consistent with other studies
370 (31, 32).

371 The distinct specificity of cleavage for RNase L (UA \downarrow , UU \downarrow and UC \downarrow sequences) and EndoU
372 (U \downarrow A and C \downarrow A sequences) allowed us to compare the relative amounts of each enzyme activity
373 in the various experimental conditions. MHV RNAs were cleaved predominantly by EndoU
374 activity within MHV^(S)-infected and MHV^(V)-infected BMM (Fig. 4A and D). MHV RNA was
375 cleaved by both RNase L and EndoU activities within PDE^{mut}-infected WT BMM while MHV RNA

376 was cleaved predominantly by RNase L activity within EndoU^{mut}-infected WT BMM (Fig. 4A and
377 D). The activation of RNase L within PDE^{mut}-infected and EndoU^{mut}-infected WT BMM was
378 expected, as these viral proteins coordinately block the OAS-RNase L pathway (22, 26, 28, 29).
379 Dinucleotide analysis of positions downstream from cleavage sites confirmed a strong
380 preference for adenine 3' of the cleavage positions in MHV RNA in WT BMM (Figs. S2A and
381 S2B). When EndoU was inactivated within EndoU^{mut}-infected cells, the strong preference for
382 adenine 3' of cleavage positions in MHV RNA was dramatically reduced, but not entirely
383 eliminated in WT BMM (Fig. S2A), IFNAR^{-/-} BMM (Fig. S3A) and RNase L^{-/-} BMM (Fig. S3B).
384 The residual cleavage of MHV RNA within EndoU^{mut}-infected RNase L^{-/-} BMM is likely due to
385 angiogenin or another RNase A family member, as these enzymes are present within
386 macrophage and they share a predilection for cleavage at U[↓]A and C[↓]A sequences (61-64).
387 We identified cyclic phosphate cDNAs dependent on the presence of either RNase L or EndoU
388 and then used fold-change to identify and assign specific sites as RNase L or EndoU targets
389 (Fig. 3 and Fig. S4). We determined how many of these sites could be assigned to either
390 endoribonuclease for each experimental condition (Fig 3). EndoU cleaved MHV RNA at both 9
391 and 12 hpi in all three cell types, with increased amounts of cleavage at 12 hpi as compared to
392 9 hpi (Fig. 3A, B and C). MHV RNA was cleaved by RNase L activity at both 9 and 12 hpi in WT
393 BMM, with exacerbated amounts of RNase L activity in PDE^{mut}-infected and EndoU^{mut}-infected
394 WT BMM, as expected. In EndoU^{mut}-infected WT BMM, there were nearly equal numbers of
395 cleavage sites assigned to RNase L at 9 and 12 hpi, which was not observed in any other
396 condition (Fig. 3A). By comparison with WT BMM, less RNase L-dependent cleavage was
397 detected in IFNAR^{-/-} BMM (Fig. 3B), consistent with reduced OAS expression and reduced
398 RNase L activity in IFNAR^{-/-} BMM (65). Additionally, the number of sites assigned to EndoU in
399 IFNAR^{-/-} and RNase L^{-/-} BMM was less than that observed in WT BMM, suggesting that EndoU
400 activity was altered in the absence of IFN signaling and innate immune effectors (Fig. 3A and

401 3B). We attributed the majority of endoribonuclease cleavage sites within MHV RNA to either
402 EndoU (U \downarrow A and C \downarrow A sequences) or RNase L (UA \downarrow , UU \downarrow and UC \downarrow sequences) activities (Figs.
403 3 and 4); however, undefined enzymes cleaved MHV RNA within EndoU^{mut}-infected RNase L^{-/-}
404 BMM (Fig. 3C). As mentioned above, the residual cleavage of MHV RNA within EndoU^{mut}-
405 infected RNase L^{-/-} BMM was likely due to angiogenin or another RNase A family member, as
406 these enzymes are present within macrophage and they share a predilection for cleavage at
407 U \downarrow A and C \downarrow A sequences (61-64). The patterns and amounts of EndoU-dependent and RNase
408 L-dependent cleavage in MHV RNA were consistent from one experiment (Figs. 3 and 4) to
409 another (Figs. S8B-S8F).

410 It is intriguing to note that EndoU and RNase L share a common substrate dinucleotide, UA.
411 Furthermore, we can distinguish between cleavage of UA by EndoU and RNase L as these
412 enzymes cleave the UA sequence at distinct sites: EndoU cleaves between U \downarrow A sequences
413 whereas RNase L cleaves after UA \downarrow dinucleotides (Fig. 4H). We found hundreds of UA
414 sequences in MHV RNA cleaved by both EndoU and RNase L (Fig. 4G). EndoU activity
415 predominated in MHV^(S)-infected and MHV^(V)-infected WT BMM at 9 and 12 hpi (Fig. 4G, MHV^(S)
416 and MHV^(V)). Yet in PDE^{mut}-infected WT BMM, either EndoU or RNase L cleaved about half of
417 the UA sequences that were targeted by both enzymes (Figs. 4G and S8F, PDE^{mut}). EndoU
418 cleaved to a greater extent about half of the shared sites whereas RNase L cleaved another half
419 to a greater extent (Figs. 4G and S8F, PDE^{mut}). Thus, while EndoU and RNase L have
420 overlapping sequence specificity and share common UA targets within MHV RNAs, these
421 enzymes do not tend to cleave the same molecule at the same site at any one moment in time.
422 Our data show that the majority of cleavage of MHV RNA was from EndoU rather than RNase L
423 during WT MHV infections (Figs. 4G and S8F, WT); however, when the MHV PDE was mutated,
424 a much larger proportion of cleavage events in viral RNA were from RNase L (Figs. 4G and S8F,
425 PDE^{mut}).

426 Taken together, these data indicate that EndoU and RNase L cleaved MHV RNA within infected
427 BMMs. The majority of endoribonuclease cleavage sites within MHV RNA were attributed to
428 either EndoU (U \downarrow A and C \downarrow A sequences) or RNase L (UA \downarrow , UU \downarrow and UC \downarrow sequences) activities
429 (Figs. 3 and 4). However, data from EndoU^{mut}-infected RNase L^{-/-} BMM (Fig. 3C) indicate that
430 viral RNA was cleaved by other undefined endoribonucleases as well. Furthermore, when MHV
431 NS2 PDE or nsp15 EndoU were inactivated by mutations, RNase L activity was much greater,
432 with increased cleavage of MHV RNA by RNase L. Thus, both MHV NS2 PDE and nsp15
433 EndoU activities prevent MHV RNA cleavage by the dsRNA-activated OAS/RNase L pathway,
434 confirming our previous reports (26, 28, 29).

435 **RNase L-dependent and EndoU-dependent cleavage sites in MHV RNA.** A fold-change
436 analysis was used to compare the magnitudes of RNase L-dependent and EndoU-dependent
437 cleavage at each base of MHV RNA across experimental conditions (Fig. 5A). By subtracting
438 endoribonuclease cleavage events detected for each virus in RNase L^{-/-} BMM, we identified the
439 top 100 RNase L-dependent cleavage sites in MHV RNA (Fig. 5B). By subtracting the
440 endoribonuclease cleavage events detected for the EndoU^{mut}, we identified the top 100 EndoU-
441 dependent cleavage sites in MHV RNA (Fig. 5C).

442 RNase L-dependent sites in MHV RNA were cleaved at the greatest magnitudes in PDE^{mut}-
443 infected and EndoU^{mut}-infected WT BMM (Fig. 5B). RNase L-dependent cleavage of MHV RNA
444 was substantially lower in IFNAR^{-/-} cells, as expected (65), especially that associated with
445 infections by the PDE^{mut} and EndoU^{mut} (Fig. 5B). The top 15 RNase L-dependent cleavage sites
446 in MHV RNA were at UA \downarrow , UU \downarrow and UG \downarrow dinucleotides distributed across the viral genome, with
447 a clustering of sites within the first 2/3 of the genome (Fig. 5D). Magnitudes of cleavage at each
448 of these sites ranged from 0.05 to 0.08% of all cleavage sites in each cDNA library (~1/2000
449 cleavage sites in the cDNA library). Together, these top 15 cleavage sites in MHV RNA
450 accounted for ~1% of all cleavage sites in this cDNA library, across all host and viral RNAs.

451 These data indicate that RNase L cleaved coronavirus RNA most efficiently at a relatively small
452 number of sites in the viral genome.

453 EndoU-dependent cleavage sites in MHV RNA were evident in WT, IFNAR^{-/-} and RNase L^{-/-}
454 BMMs; however, EndoU cleaved MHV RNA to a greater extent in WT BMM (Fig. 5C). Subdued
455 magnitudes of EndoU-dependent cleavage of MHV RNA were observed at 12 hpi in IFNAR^{-/-}
456 and RNase L^{-/-} cells, as compared to WT BMM, suggesting a potential functional interaction
457 between EndoU and dsRNA-activated host responses, or RNase L in particular. Additionally,
458 most of the sites with EndoU-dependent cleavage activity had similar magnitudes of change,
459 leading to a uniform distribution of sites across all conditions, excluding a few outliers. The top
460 15 EndoU-dependent cleavage sites in MHV RNA were at C[↓]A and U[↓]A sequences distributed
461 to a greater extent in the last 2/3 of the viral genome (Fig. 5E).

462 We examined the cumulative distribution of cleavage in MHV RNA, across all conditions (Figs.
463 5F and S8E). In this analysis, we plotted the overall accumulation of cyclic phosphate reads as
464 a function of position along the MHV genomic RNA (Figs. 5F and S8E). Because RNase L-
465 dependent cleavage sites (Fig. 5D) and EndoU-dependent cleavage sites (Fig. 5E) were
466 distributed across the MHV RNA genome in WT BMM, cumulative cleavage increased from 0%
467 at the 5' end of the genome to 100% at the 3' end of the genome, with a slope of ~45° for
468 MHV^(S) and MHV^(V) in WT BMM [Fig. 5F, WT BMM, green and blue lines for MHV^(S) and MHV^(V)].
469 In EndoU^{mut}-infected WT BMM, cleavage of MHV RNA increased in the ORF1a and ORF1b
470 regions of the genome as compared to MHV^(S) and MHV^(V), shifting the slope of cumulative
471 cleavage to the left (Fig. 5F, WT BMM, red line for EndoU^{mut}). In contrast, when both EndoU and
472 RNase L activities were absent, as in EndoU^{mut}-infected RNase L^{-/-} BMM, cleavage of MHV
473 RNA was substantially reduced across most of the genome, with a spike of EndoU- and RNase
474 L-independent cleavage near the 3' UTR (Fig. 5F, RNase L^{-/-} BMM, red line for EndoU^{mut}). Note
475 how the slope of the line for EndoU^{mut} goes from ~50% to 100% of cumulative cleavage

476 between nucleotides 30,000 and 31,344. This indicates that endoribonucleolytic cleavage was
477 much more pronounced near the 3' terminus of MHV RNA in EndoU^{mut}-infected IFNAR^{-/-} and
478 RNase L^{-/-} BMM, as compared to WT BMM. These data indicate that EndoU^{mut} MHV RNA was
479 cleaved at very different magnitudes from one end to the other in WT BMM versus that in
480 RNase L^{-/-} BMM, with increased relative amounts of cleavage between nts 1-20,000 in WT BMM,
481 less cleavage between nts 1-30,000 in RNase L^{-/-} BMM, and a spike in cumulative cleavage
482 near the 3' terminus in RNase L^{-/-} BMM.

483 These data also indicate that EndoU and RNase L account for a substantial amount of the
484 cumulative cleavage in the orf1a and orf1b regions of the MHV RNA genome. MHV RNA was
485 cleaved to a greater extent within orf1a and orf1b in WT BMM, especially when EndoU was
486 disabled (Fig. 5F, red line for EndoU^{mut} shifts to the left in WT BMM). Conversely, MHV RNA
487 was cleaved to a lower extent within orf1a and orf1b in RNase L^{-/-} BMM, especially when EndoU
488 was disabled (Fig. 5F, red line for EndoU^{mut} shifts to the right in RNase L^{-/-} BMM). When EndoU
489 and RNase L activities were absent, as in EndoU^{mut}-infected RNase L^{-/-} BMM, the residual
490 cleavage of MHV RNA by unspecified endoribonucleases occurred predominantly near the 3'
491 terminus of the viral genome.

492 **Endoribonuclease cleavage sites in distinct MHV RNA sequences and structures.** We
493 next examined the frequency of endoribonuclease cleavage in distinct regions of MHV RNA
494 (Figs. 6 and S7). The cumulative amounts of cleavage in each region of MHV RNA were plotted
495 unadjusted (Fig. 6A) or adjusted for both RNA abundance and size (Fig. 6B). In supplemental
496 data we show cleavage adjusted for RNA abundance alone (Fig. S7A) or size alone (Fig. S7B).
497 Cleavage was detected in every region of MHV RNA, from the 5' NTR to the 3' NTR, including
498 relatively small TRS sequences (Figs. 6A and 6B). The vast majority of cleavage events
499 occurred in 1a/1b, S and N open reading frames (Fig. 6A). When adjusted for MHV RNA
500 abundance, cleavage was most frequent in the ORF 1a/1b region and the ns2, HE and S ORFs

501 (S7A). Furthermore, with adjustments for size and abundance (Figs. 6B), one can see that
502 each of the TRS elements was targeted for cleavage at frequencies similar to that observed in
503 Orf1a/1b. Thus, although TRS sequences are quite small, they were cleaved just as frequently
504 as RNA sequences in other regions of MHV RNA. Intriguingly, TRS6 was targeted more
505 frequently (by EndoU) than other regions of MHV RNA, including other TRS elements (Fig. 6C).
506 TRS6, with a UCCAAAC sequence, is distinct from other TRS elements, which possess
507 UC \downarrow AAAC sequences. We detected the most robust EndoU-dependent cleavages at C \downarrow A and
508 U \downarrow A dinucleotides of TRS elements 4, 6, and 7 (Fig. 6C). In TRS elements 4 and 6, cleavage at
509 the very 3'-end of the TRS sequence was dependent on the presence of a downstream adenine
510 outside of the TRS sequence (Fig. 6C). Interestingly, the upstream C \downarrow A cleavage site in TRS 6
511 (Fig. 6C) relies on one of the single nucleotide polymorphisms (28960 T > C) that we detected
512 in the viral genomes (Table S3). In vitro studies using purified EndoU show cleavage of a U \downarrow A
513 dinucleotide within a TRS substrate (23). Our data indicate that C \downarrow A and U \downarrow A dinucleotides of
514 TRS elements are physiologic targets of EndoU.

515 RNAseq was used to measure the abundance of MHV RNA in all experimental conditions (Figs.
516 S5 and 6D). MHV RNA was abundant in all samples from virus-infected cells, with similar
517 amounts of MHV RNA across conditions, but for EndoU^{mut}-infected WT BMM at 9 and 12 hpi
518 (Fig. S5A). Decreased amounts of EndoU^{mut} RNA in WT BMM (Fig. S5A) correlated with
519 decreased virus replication in EndoU^{mut}-infected WT BMM at 9 and 12 hpi (26). RNAseq reads
520 were detected across the MHV RNA genome, with the most abundant reads corresponding to
521 leader sequences at the 5' end of the genome and sg mRNA sequences at the 3' end of the
522 genome (Fig. S5B). Consistent with published studies (53), MHV mRNA7 was most abundant,
523 accounting for 70 to 80% of MHV mRNAs (Figs. 6D and S9C). MHV mRNAs 1-7 were present
524 in all conditions, with some changes in relative amounts from one condition to another (Figs. 6D
525 and S9C). MHV mRNA1 (genomic RNA) was increased proportionally to other MHV mRNAs in

526 EndoU^{mut}-infected WT BMM at 12 hpi. MHV mRNA 7 was increased relative to other MHV
527 mRNAs at 12 hpi in EndoU^{mut}-infected IFNAR^{-/-} BMM and RNase L^{-/-} BMM. Remarkably, MHV
528 RNA abundance did not correlate with the frequency of cyclic phosphate reads in viral RNA
529 (Figs. S11A & S11B). Altogether, these data indicate that MHV RNA replication was able to
530 produce each of the MHV mRNAs in proportional amounts, despite considerable changes in
531 endoribonuclease activity from one condition to another.

532 Endoribonuclease cleavage sites were detected in functional RNA sequences and structures,
533 including the Orf1a/1b frameshift element and the MHV 3' NTR (Fig. 7). The Orf1a/1b frameshift
534 element contains both RNase L-dependent and EndoU-dependent cleavage sites (Figs. 7A and
535 7B). Likewise, the MHV 3' NTR contains both RNase L-dependent and EndoU-dependent
536 cleavage sites (Fig. 7C). The MHV 3' NTR spans nucleotide 31034, adjacent to the N stop
537 codon, to nucleotide 31334, adjacent to the poly(A) tail (Fig. 7C). Functional RNA sequences
538 and structures within the 3' NTR include an essential bulged stem-loop (nts 31034-31100), an
539 essential pseudoknot (nts 31101-31150), a non-essential hypervariable region (HVR) (nts
540 31179-31288), a polyadenylation signal (nts 31293-31298) and a poly(A) tail (66-68). A number
541 of EndoU-dependent cleavage sites were detected within the 3' NTR, including prominent
542 cleavage sites immediately adjacent to the poly(A) tail (Fig. 7C, ³¹³³²C \downarrow AC \downarrow A³¹³³⁵). Together,
543 these two cleavage sites account for ~0.15% of all cleavage sites in the cDNA library for the WT
544 MHV in WT BMM at 12 hpi, corresponding to ~1/677 cleavage sites in the entire cDNA library.

545 When EndoU was inactivated by an H277A mutation, the cleavage of MHV RNA at the
546 ³¹³³²C \downarrow AC \downarrow A³¹³³⁵ sequences adjacent to the poly(A) tail was dramatically reduced, but not
547 entirely eliminated, in WT BMM (Fig. S6A). Furthermore, there was EndoU-independent
548 cleavage of MHV RNA at the ³¹³³²C \downarrow AC \downarrow A³¹³³⁵ sequence in IFNAR^{-/-} BMM (Fig. S6B) and
549 RNase L^{-/-} BMM (Fig. S6C). Cleavage of MHV RNA at the ³¹³³²C \downarrow AC \downarrow A³¹³³⁵ sequences adjacent
550 to the poly(A) tail were notable whether unadjusted (Fig. S6A-C) or adjusted for RNA

551 abundance (Fig. S6D-F). These data indicate that the ³¹³³²C \downarrow AC \downarrow A³¹³³⁵ sequence in MHV RNA
552 was susceptible to both EndoU-dependent and EndoU-independent cleavage. The EndoU-
553 dependent cleavage of the ³¹³³²C \downarrow AC \downarrow A³¹³³⁵ sequence in MHV RNA was substantially greater
554 than the EndoU-independent cleavage in WT BMM (Fig. S6A); however, substantial amounts of
555 EndoU-independent cleavage were detected at the ³¹³³²C \downarrow AC \downarrow A³¹³³⁵ sequence in IFNAR^{-/-} BMM
556 (Fig. S6B) and RNase L^{-/-} BMM (Fig. S6C).

557 **Cleavage of rRNA and changes in host gene expression.** Because RNase L cleaves 18S
558 rRNA at specific sites in human cells (31, 32), we examined RNase L-dependent cleavage of
559 18S rRNA within MHV-infected murine BMMs (Figs. 8A, 8B and S10). A fold-change analysis
560 was used to compare the magnitudes of RNase L-dependent cleavage at each base of 18S
561 rRNA across experimental conditions (Fig. 8A). By subtracting endoribonuclease cleavage
562 events detected for each virus in RNase L^{-/-} BMM, we identified the top 100 potential RNase L-
563 dependent cleavage sites in MHV RNA (Fig. 8B). Four RNase L-dependent cleavage sites were
564 clearly evident in 18S rRNA: UU⁵⁴², UU⁵⁴³, UU⁷⁷¹ and UA⁷⁷². These sites, on the surface of 18S
565 ribosomal subunits, are analogous to RNase L-dependent cleavage sites in human 18S
566 subunits (31, 32). 18S rRNA was cleaved at these sites to a significant magnitude in PDE^{mut}-
567 infected and EndoU^{mut}-infected WT BMM (Figs. 8A, 8B and S10). 18S rRNA was not cleaved at
568 significant magnitudes within mock-infected BMM nor in IFNAR^{-/-} or RNase L^{-/-} BMM (Fig. 8A
569 and 8B). Thus, as in human cells (31, 32), RNase L targets 18S rRNA for cleavage at precise
570 sites in murine cells. Furthermore, RNase L activity was specifically increased within PDE^{mut}-
571 infected and EndoU^{mut}-infected WT BMM, as compared to MHV^(S)-infected and MHV^(V)-infected
572 WT BMM (Fig. 8A and 8B). Although RNase L-dependent cleavage sites in rRNA were easily
573 detected (Figs. 8A, 8B and S10), EndoU-dependent cleavage sites in rRNA were not detected
574 (Fig. S10B). These data show the dsRNA-dependent OAS/RNase L pathway was significantly
575 activated in PDE^{mut}- and EndoU^{mut}-infected WT BMM, and exclude rRNAs as targets of EndoU.

576 dsRNA-dependent host gene expression was also increased within MHV-infected WT BMM (Fig.
577 8C-E). We used a Volcano plot (Fig. 8C) and gene ontology (GO) analyses to classify the
578 nature of host gene expression within MHV-infected WT BMM (Fig. 8D and 8E) (49, 50). The
579 Volcano plot shows the expression of many genes increasing by 2² to 2¹⁰-fold / 4-fold to 1024-
580 fold (Fig. 8C). Increased gene expression in MHV^(S)-infected WT BMM corresponded to a
581 number of biological processes: negative regulation of apoptosis, LPS-activated gene
582 expression, positive regulation of GTPase activity and IFN-gamma activated gene expression
583 (Fig. 8D). Increased gene expression in EndoU^{mut}-infected WT BMM (Fig. S12A and S12B)
584 corresponded to some of these same groups of host genes, with a notable addition, response to
585 exogenous dsRNA (Fig. 8E). Thus, GO analysis indicated that host gene expression associated
586 with response to exogenous dsRNA was specifically activated in EndoU^{mut}-infected WT BMM,
587 as compared to MHV^(S)-infected WT BMM (Fig. 8D and 8E).

588 Because GO analysis implicated “response to exogenous dsRNA”, we examined the
589 magnitudes of expression for each host gene in this gene ontology group: GM13272, GM13283,
590 IFN-alpha genes, IFN-beta, IFN-Z, Nfkbia, Nod2, Ripk2 and Tlr3 (Fig. 8E). We compared
591 magnitudes of expression in mock-infected, MHV^(S)-infected, MHV^(V)-infected, PDE^{mut}-infected
592 and EndoU^{mut}-infected WT BMM (Fig. 8E). Host gene expression associated with response to
593 dsRNA increased by 100- to 1000-fold in MHV-infected WT BMM as compared to mock-infected
594 cells, with even larger 1000- to 10,000-fold increases in EndoU^{mut}-infected WT BMM (Fig. 8E).
595 Thus, host genes associated with response to dsRNA were notably increased in MHV-infected
596 BMM, with the greatest increases occurring within EndoU^{mut}-infected WT BMM (Fig. 8E). Genes
597 upregulated or downregulated in MHV^(S)-infected cells did not vary substantially between WT
598 and RNase L^{-/-} BMM (Fig. 8F and 8G). Altogether, these data indicate that dsRNA-dependent
599 host responses were exacerbated within MHV-infected cells, especially in EndoU^{mut}-infected WT
600 BMM. These data are consistent with recent studies from the Baker lab (69).

601 **Cellular endoribonucleases.** The residual cleavage of MHV RNA within EndoU^{mut}-infected
602 RNase L^{-/-} BMM provoked our consideration of other cellular endoribonucleases. We
603 hypothesized that residual pyrimidine specific cleavage of MHV RNA might be due to one or
604 another RNase A family enzyme (63). We also considered T2 endoribonucleases based on their
605 reported contributions to TLR8 activation (70). Consequently, we examined the expression of
606 RNases 4 and 5 (angiogenin) and RNases T2A and T2B (Fig. S12C). Changes in magnitudes of
607 RNase 4 and 5 expression were observed, with ~10-fold decreased expression in MHV^(S)-
608 infected and MHV^(V)-infected WT BMM as compared to Mock-infected WT BMM (Fig. S12C).
609 Decreased expression of RNases 4 and 5 was not as strong in PDE^{mut}-infected WT BMM, and
610 very little decrease in expression was observed in EndoU^{mut}-infected WT BMM. Similar changes
611 in expression of RNases 4 and 5 were observed in IFNAR^{-/-} BMM and RNase L^{-/-} BMM, with
612 significantly decreased expression in MHV^(S)-infected and MHV^(V)-infected cells and a more
613 limited decrease in EndoU^{mut}-infected cells (Fig. S12C). Because RNases 4 and 5 share a
614 complex dual promoter (71), with alternative splicing leading to the expression of either RNase 4
615 or RNase 5, coordinate increases and decreases in their expression was not unexpected.
616 These data reinforce our suspicion regarding the residual pyrimidine specific cleavage of MHV
617 RNA within EndoU^{mut}-infected RNase L^{-/-} BMM.

618 In contrast to expression of RNase 4 and 5, changes in magnitudes of expression of RNases
619 T2A and T2B were relatively small within MHV-infected cells, with a tendency for slightly
620 increased expression (Fig. S12C). RNase T2 cleaves RNA within endosomes and lysosomes,
621 targeting purine:uridine dinucleotides, R^ψU (70). The residual purine specific cleavage of MHV
622 RNA within EndoU^{mut}-infected RNase L^{-/-} BMM might be associated with RNase T2 activity;
623 however, our experiments do not definitively address this possibility.

624 **DISCUSSION**

625 We address a key question in the coronavirus field (72): What is the natural target of EndoU?
626 Coronavirus EndoU prevents dsRNA-activated antiviral responses in infected cells (26);
627 however, it is not clear how EndoU does this because its physiologic RNA substrates are
628 unknown. In this study, we used MHV-infected bone marrow-derived macrophage (BMM) and
629 cyclic phosphate cDNA sequencing to identify the RNA targets of EndoU.

630 We found that EndoU targeted MHV RNA within infected cells, cleaving viral RNA on the 3' side
631 of pyrimidines with a strong preference for cleavage between U[↓]A and C[↓]A sequences
632 (endoY[↓]A) (Fig. 4). This cleavage specificity from MHV-infected cells is consistent with that of
633 purified EndoU (23, 60) and RNase A (61, 62), enzymes that are functionally and structurally
634 related to one another (7). EndoU cleavage was detected in every region of MHV RNA, from
635 the 5' NTR to the 3' NTR, including relatively small TRS sequences (Figs. 5E, 6 and 7).

636 Because MHV RNA is a template for both viral mRNA translation and viral RNA replication,
637 cleavage by EndoU could inhibit both of these biosynthetic processes (Fig. 9). Intriguingly, MHV
638 TRS sequences contain EndoU target sequences (C[↓]A and U[↓]A sequences) (Fig. 6C). TRS6,
639 which was targeted more frequently by EndoU than other TRS elements, contains a C[↓]A target
640 sequence rather than a U[↓]A sequence. We postulate that EndoU cleaves MHV RNA in a
641 regulated manner, to inhibit negative-strand RNA synthesis, thereby preventing the
642 accumulation of viral dsRNA (Fig. 9). Nsp16 (2' O-MT) could regulate EndoU-mediated
643 cleavage of MHV RNA by methylating C[↓]A and U[↓]A sequences (1).

644 **How does EndoU inhibit double-stranded RNA-activated antiviral responses?** Coronavirus
645 EndoU prevents the activation of multiple host dsRNA sensors, including MDA5, OAS and PKR
646 (22, 26, 27). dsRNA-activated OAS/RNase L and PKR pathways restrict the replication of
647 EndoU-deficient coronaviruses (26). Because EndoU^{mut}-infected cells had increased
648 accumulation of dsRNA, Kindler and colleagues (26) concluded that EndoU functions as a viral

649 RNA decay pathway to evade dsRNA-activated antiviral host cell responses. Consistent with
650 this idea, Hackbart et al. (73) report that EndoU targets poly(U) sequences at the 5' end of viral
651 negative-strand RNA. Another report suggests that EndoU might control the localization of viral
652 dsRNA within cells, perhaps maintaining dsRNA within membranous RNA replication complexes
653 (22). Our data suggest a third possibility, that EndoU targets MHV RNA to prevent the synthesis
654 of dsRNA (Fig. 9): EndoU-dependent cleavages were detected throughout the genomic RNA
655 (Figs. 5E, 6 and 7), indicating that EndoU destroys the template for negative-strand RNA
656 synthesis, precluding the formation of dsRNA, rather than acting on dsRNA. Cyclic phosphate
657 cDNA sequencing detected large amounts of cleavage in MHV (+) strand (Fig. 2 and Fig. 8SA)
658 and vanishing little cleavage in MHV (-) strand (Figs. S1B, S11C-D). Cyclic phosphate cDNA
659 sequencing can readily detect cleavage sites in both (+) and (-) strands of viral RNA (31, 32);
660 however, cleavage of poly(U) sequences at the 5' end of MHV negative-strand RNA cannot be
661 detected because the resulting cyclic phosphate RNA fragments are too small (<20 bases long)
662 and they are homopolymeric, preventing detection by our sequencing and bioinformatics
663 pipelines. While it is possible that EndoU targets poly(U) sequences, the specificity of EndoU for
664 C^ψA and U^ψA sequences in vivo (Fig. 4) is inconsistent with poly(U) substrates being
665 physiologically relevant. Furthermore, purified EndoU (60) and RNase A (61, 62) readily target
666 UA sequences within heteropolymeric substrates. Thus, we conclude that EndoU targets MHV
667 (+) strand RNA to prevent the synthesis of dsRNA (Fig. 9). Nonetheless, potential RNA
668 substrates in (+) and (-) strands are not mutually exclusive. EndoU-dependent cleavage of the
669 CACA sequences at the 3' end of the (+) strand and the poly(U) at the 5' end of the (-) strand
670 could occur coordinately, as both are co-localized adjacent to one another at the same end of
671 dsRNA products. When EndoU was mutated, we detected the activation of the dsRNA-
672 dependent OAS/RNase L pathway (Figs. 4, 5 and 8) and increased host gene expression
673 associated with response to dsRNA (Figs. 8D and 8E). These data, like other reports (22, 26, 27,
674 69), indicate EndoU prevents the activation of dsRNA sensors.

675 EndoU cleaved MHV RNA in every region of the genome (Figs. 5E, 6 & 7). Because MHV RNA
676 is a template for both viral mRNA translation and viral RNA replication, cleavage by EndoU
677 could inhibit both of these biosynthetic processes (Fig. 9). Cleavage of the viral genome would
678 prevent the expression of the viral replicase. Coronavirus RNA synthesis requires ongoing
679 expression of the viral replicase, with negative-strand RNA synthesis being most dependent on
680 new replicase expression (74). Substantial amounts of EndoU-dependent cleavage were
681 detected in orfs 1a and 1b, especially within WT BMM (Fig. 5), potentially limiting the expression
682 of replicase. Cleavage of MHV genomic RNA, the template for both genomic and subgenomic
683 negative-strand RNA synthesis (10), would also prevent the synthesis of dsRNA products (Fig.
684 9). EndoU-mediated cleavage of the tandem CA sequences adjacent to the MHV RNA poly(A)
685 tail is most intriguing in this regard (Figs. 7C and S6). The CA sequences adjacent to the MHV
686 RNA poly(A) tail are conserved in group 2 coronaviruses, present in both genomic and sg
687 mRNAs, and positioned adjacent to the poly(A) template used for the initiation of negative-
688 strand RNA synthesis (68). The coronavirus polymerase, nsp12, with nsp7 and 8 cofactors (75),
689 initiates negative-strand RNA synthesis on the poly(A) tail of genomic RNA, leading to the
690 synthesis of poly(U) at the 5' end of negative-strand RNA. Because coronavirus nsp12 is a
691 primer-dependent RNA polymerase (76), nsp8 is thought to prime negative-strand RNA
692 synthesis (77), making a poly(U) product from the poly(A) tail of genomic RNA templates (16).
693 Cleavage of the tandem CA sequences adjacent to the MHV RNA poly(A) tail would disrupt
694 negative-strand RNA synthesis at the point of initiation. This provides a theoretically appealing
695 mechanism for EndoU and other endoribonucleases to prevent the synthesis of dsRNA (Fig. 9).
696 MHV RNA was cleaved by one or more unspecified endoribonucleases in EndoU^{mut}-infected
697 RNase L^{-/-} BMM. Thus, in addition to EndoU- and RNase L-dependent cleavage of MHV RNA,
698 we observed EndoU- and RNase L-independent cleavage of MHV RNA (Fig. 2 and Fig. S8). By
699 using fold-change analyses between wt and mutant conditions, we attributed the majority of

700 endoribonucleolytic cleavage sites in MHV RNA to EndoU activity and RNase L activity (Fig. 5);
701 however, a substantial amount of cleavage in MHV RNA persisted in EndoU^{mut}-infected RNase
702 L^{-/-} BMM (Fig. 2, EndoU^{mut}, red bars). More than 5% of the cyclic phosphates in EndoU^{mut}-
703 infected RNase L^{-/-} BMM RNA samples were in MHV RNA (Fig. 2, EndoU^{mut}, red bars). This
704 EndoU- and RNase L-independent cleavage of MHV RNA occurred predominantly at UA and
705 CA dinucleotides (Fig. 4D); especially within IFNAR^{-/-} (Fig. S3A, Position -1 to +1) and RNase L^{-/-}
706 (Fig. S3B, Position -1 to +1) BMM. Thus, the EndoU- and RNase L-independent cleavage of
707 MHV RNA exhibited a nucleotide specificity similar to that of EndoU-dependent cleavage. It is
708 possible that the H277A mutation in EndoU fails to completely inhibit endoribonuclease activity;
709 however, we suspect that RNase A family members are responsible for this residual EndoU-
710 independent cleavage of MHV RNA at U \downarrow A and C \downarrow A sequences. RNase A family enzymes are
711 expressed in macrophage (63) and they cleave RNA at U \downarrow A and C \downarrow A sequences (62, 64).
712 EndoU-independent cleavage of MHV RNA at the ³¹³³²C \downarrow AC \downarrow A³¹³³⁵ sequence was evident in
713 WT BMM (Fig. S6A), IFNAR^{-/-} BMM (Fig. S6B) and RNase L^{-/-} BMM (Fig. S6C). The expression
714 of RNases 4 and 5 (Fig. S12C) is consistent with residual cleavage at the ³¹³³²C \downarrow AC \downarrow A³¹³³⁵
715 sequences in EndoU^{mut}-infected BMM (Fig. S6). These data indicate that the ³¹³³²C \downarrow AC \downarrow A³¹³³⁵
716 sequence in MHV RNA was susceptible to both EndoU-dependent and EndoU-independent
717 cleavage. The atomic structure of EndoU revealed an RNase A-like catalytic domain (6);
718 however, we did not anticipate the degree of overlap in substrate specificity observed for
719 EndoU-dependent and EndoU-independent (presumably RNase A family) enzymes within BMM.
720 Additional experiments will be required to address the identity and functional significance of the
721 EndoU-independent (presumably RNase A family) enzymes within BMM.

722 **EndoU activity and cellular RNAs.** Substantial amounts of EndoU-dependent and RNase L-
723 dependent cleavage of MHV RNA were detected (Fig. 5), along with RNase L-dependent
724 cleavage of rRNA (Figs. 8A, 8B and S10), but EndoU-dependent cleavage of cellular RNAs was

725 not evident in our datasets. EndoU-dependent cleavage sites in rRNAs would be relatively easy
726 to detect due to the abundance of rRNAs and to the well-established fold-change analyses
727 proven to detect RNase L-dependent cleavage sites. Thus, we are confident that EndoU did not
728 produce detectable cyclic phosphate moieties in rRNAs under the conditions of our experiments.
729 Whether or not EndoU targets cellular mRNAs for cleavage is less certain. The low abundance
730 of individual cellular mRNAs in our cyclic phosphate cDNA libraries precludes definitive
731 assignment of one or another endoribonuclease to individual cleavage sites in individual cellular
732 mRNAs. Thus, cellular mRNAs are cleaved by endoribonucleases, as they constitute ~5% of all
733 cleavage in our cyclic phosphate cDNA libraries (Figs. 2 and S8); however, we are not able to
734 specify which endoribonucleases are responsible for individual cleavage sites within individual
735 cellular mRNAs due to the limited abundance of any one cellular mRNA. Because EndoU-
736 dependent cleavage sites were abundant in MHV RNAs, we suspect that EndoU is localized
737 within RNA replication complexes, consistent with another report (21).

738 **Does nsp16 (2' O-MT) regulate EndoU?** Deng and Baker highlight another unanswered
739 question in the field (72): How is EndoU activity regulated to avoid unwanted cleavage
740 events? This is an important question because MHV RNA integrity is critical for viral mRNA
741 translation and viral RNA replication (Fig. 9). When EndoU cleaves MHV RNA, it must do so in a
742 regulated manner to avoid self-destruction. Residual amounts of MHV genomic RNA must be
743 maintained within infected cells to sustain an infection. One factor thought to regulate EndoU is
744 nsp16, a 2' O-methyltransferase (1).

745 When EndoU was first characterized, Ivanov and colleagues demonstrated that EndoU-
746 mediated cleavage of RNA substrates was prevented by 2'-O-methylation (1). They also
747 highlighted the modular nature of viral evolution, drawing attention to the side-by-side nature of
748 nsp15 (EndoU) and nsp16 (2' O-MT) within nidovirus genomes, suggesting a functional interplay
749 between the two enzymes (1). 2'-O-methyltransferases have been functionally characterized in

750 two families of positive-strand RNA viruses, coronaviruses (25, 78) and flaviviruses (79-82).
751 One function of these enzymes is to methylate the adenosine of 5' cap structures in viral
752 mRNAs (81), to evade the antiviral activity of IFIT1 (25, 79, 80). Whether these enzymes can
753 methylate other residues throughout viral RNA is less certain; however, 2'-O-methyltransferases
754 are reported to inhibit the recognition of viral dsRNA by MDA5 (25). It is intriguing to note that
755 EndoU cleavage sites (C^ψA and U^ψA sequences) contain adenosine. 2'-O-methylation of the
756 pyrimidine at cleavage sites would prevent cleavage of viral RNA because the 2' hydroxyl of
757 ribose is the nucleophile responsible for attacking the phosphodiester backbone (59). Whether
758 2' O methylation of adenosine can prevent EndoU-mediated cleavage of C^ψA and U^ψA
759 sequences remains to be determined; however, some amount of intact MHV genomic RNA
760 must be maintained within infected cells to sustain an infection.

761 RNAseq showed that MHV RNAs were abundant (Fig. S5) and there were proportional amounts
762 of each MHV mRNA within infected cells (Fig. 6D) despite profound changes in
763 endoribonuclease activity from one condition to another. Thus, neither EndoU nor RNase L
764 activities were associated with extreme changes in the proportions of one MHV mRNA to
765 another. Rather, relatively subtle changes in MHV mRNA1-8 proportions were observed. These
766 data suggest that EndoU and RNase L activities modulate MHV RNA abundance during
767 infections, but do not contribute to extreme changes in the relative amounts of one MHV mRNA
768 to another. In contrast, the absence of EndoU activity during MHV infection lead to profound
769 increases in host gene expression associated with response to dsRNA (Figs. 8D and 8E),
770 despite the activation of RNase L activity. Expression and translation of cellular mRNAs occurs
771 in the context of activated RNase L despite its' ongoing degradation of cellular RNAs during a
772 dsRNA-activated stress response (83, 84). Ongoing expression and translation of MHV mRNAs
773 likely occur in the context of EndoU or RNase L activities in the same manner. When pre-
774 existing host or viral mRNAs are destroyed by EndoU or RNase L activities, new MHV mRNAs

775 are synthesized to refresh the pool of viral mRNAs. Thus, MHV replication can clearly tolerate -
776 and perhaps benefit from - both EndoU and RNase L activities.

777 **Do EndoU and RNase L co-regulate MHV RNA gene expression and replication?**

778 Importantly, EndoU and RNase L share a common cleavage site, UA (Fig. 4). Furthermore, we
779 can distinguish between EndoU-dependent and RNase L-dependent cleavage of UA sequences
780 because EndoU cleaves between U \downarrow A dinucleotides whereas RNase L cleaves after UA \downarrow
781 dinucleotides. Under some conditions, such as MHV^(S)-infected and MHV^(V)-infected WT BMM,
782 UA sequences in viral RNA were cleaved predominantly by EndoU (Fig. 4G). Under other
783 circumstances UA sequences in MHV RNA were cleaved predominantly by RNase L, as in
784 PDE^{mut}-infected and EndoU^{mut}-infected WT BMM (Fig. 4G). In both cases, regardless of whether
785 the host or viral endoribonuclease cleaves MHV RNA, the consequence will be an inhibition in
786 viral mRNA translation and an inhibition in viral RNA replication (Fig. 9). It is interesting to see
787 that both a host and a viral endoribonuclease have the capacity to inhibit magnitudes of MHV
788 gene expression and replication by targeting a common set of UA sequences within the viral
789 genome. It is also interesting that EndoU activity was subdued within IFNAR^{-/-} and RNase L^{-/-}
790 cells, as if EndoU activity was modulated by RNase L activity (Fig. 5C). Together, these results
791 suggest an interesting interplay between EndoU and dsRNA-activated host responses (Fig. 9).

792 **Summary.** We addressed a key question in the field (72): What is the natural target of
793 coronavirus EndoU? We find that EndoU targets MHV RNA within infected cells, cleaving viral
794 RNA on the 3' side of pyrimidines with a strong preference for cleavage between U \downarrow A and C \downarrow A
795 sequences (endoY \downarrow A). We postulate that EndoU cleaves MHV RNA in a regulated manner, to
796 inhibit negative-strand RNA synthesis, reducing the accumulation of viral dsRNA, while ensuring
797 continuing virus replication (Fig. 9). By regulating the synthesis and accumulation of viral dsRNA,
798 coronaviruses can evade double-stranded RNA-activated antiviral responses within infected
799 cells (22, 26, 27, 72).

800 **ACKNOWLEDGMENTS**

801 We thank members of the Barton and Weiss labs for critical evaluation of the manuscript. We
802 thank Evan Lester for assistance with bioinformatics analyses. This work was supported by
803 Public Health Service grants from the National Institutes of Health (F30 AI140615 to RA,
804 AI104887 to SRW, GM119550 to JRH and AI042189 to DJB) and the Swiss National Science
805 Foundation (SNF project 149784).

806 **AUTHOR CONTRIBUTIONS**

807 Rachel Ancar: Experimental Design, Experimental Procedures, Bioinformatics, Data Analysis,
808 Data Curation, Interpretation of Data and Manuscript Preparation.

809 Yize Li: Experimental Design, Experimental Procedures and Interpretation of Data.

810 Eveline Kinder: Experimental Design and Experimental Procedures.

811 Daphne Cooper: Methodology and Pilot Study.

812 Monica Ransom: Experimental Procedures.

813 Volker Thiel: Experimental Design, Project Administration, Funding Acquisition and Data
814 Interpretation.

815 Susan Weiss: Experimental Design, Project Administration, Funding Acquisition and Data
816 Interpretation.

817 Jay Hesselberth: Experimental Design, Project Administration, Funding Acquisition and Data
818 Interpretation and Manuscript Preparation.

819 David Barton: Experimental Design, Project Administration, Funding Acquisition, Data
820 Interpretation and Manuscript Preparation.

821 **Competing Interests:** Authors report no competing interests.

822 **FIGURE LEGENDS**

823 **Figure 1. Coronavirus RNA genome and Experimental Approach.** (A) MHV RNA genome
824 highlighting two mutations: His to Arg mutation in the MHV phosphodiesterase domain active
825 site (PDE^{H126R}), and a His to Ala mutation in the MHV EndoU-domain active site (EndoU^{H277A})
826 (26, 38). MHV proteins are categorized as nonstructural (light grey), accessory (dark gray) and
827 structural (black). (B) Bone marrow-derived macrophage (BMM) from WT, IFNAR^{-/-}, and RNase
828 L^{-/-} mice were mock-infected or infected with WT MHV [MHV^(S) and MHV^(V)], the PDE^{mut}, or
829 EndoU^{mut} for 9 and 12 hours (26, 29), after which total cellular RNA was isolated for cyclic
830 phosphate sequencing. (C) Schematic of cyclic phosphate sequencing, protocol adapted from
831 Schutz et al., 2011 (34).

832 **Figure 2. Frequency of endoribonuclease cleavage in host and viral RNAs.** (A and B)
833 Normalized cyclic phosphate cDNA reads ([reads at each position / total reads in library])
834 mapped to host and viral RNAs at 9 and 12 hpi in WT, IFNAR^{-/-}, and RNase L^{-/-} bone marrow
835 macrophages (BMM).

836 **Figure 3. Frequency and location of endoribonuclease cleavage sites in MHV genomic**
837 **RNA.** (A and B) Normalized cyclic phosphate cDNA reads captured at each position along the
838 MHV genomic RNA at 9 and 12 hpi with MHV^(S), MHV^(V), PDE^{mut}, and EndoU^{mut} virus in (A) WT
839 BMM, (B) IFNAR^{-/-}, and (C) RNase L^{-/-} BMM. Putative cleavage sites attributed to EndoU or
840 RNase L were calculated from RNase L- or EndoU-dependent signal generated by subtracting
841 signal from each captured position that occurs in the absence of either enzyme (RNase L^{-/-}
842 BMM or during EndoU^{mut} infection). These data were then filtered for sites with reads
843 representing at least 0.01 % of total reads in the library. At each of these positions, the log₂ fold
844 change in signal when either RNase L or EndoU were absent was calculated and sites with ≥
845 2.5 fold change were designated putative RNase L or EndoU sites.

846 **Figure 4. Dinucleotide endoribonuclease cleavage preference of MHV genomic RNA.** (A
847 and D) Dinucleotide specificity analysis for cleavage in MHV genomic RNA by percent total
848 cDNA reads captured at each 3'-dinucleotide in WT BMM at 9 and 12 hpi for (A) Dinucleotide
849 analysis for positions -2: -1 and (D) Dinucleotide analysis for positions -1:+1 from captured
850 cleavage position (0 position). (B and E). Dinucleotide enrichment for dinucleotide positions
851 from -2: -1 (B) or -1: +1 (E) for each condition of viral infection at 12 hpi in WT BMM by
852 comparing the frequency of dinucleotide capture in experimental conditions to the frequency of
853 occurrence for each dinucleotide in the MHV genomic RNA sequence (control). Significant
854 enrichment was determined by adjusted p-value (q) for fold change ($[\log_2(\text{experiment} / \text{control})]$).
855 ($<0.02^*$, $<0.0001^{**}$, $<1 \times 10^{8****}$). Only dinucleotides with positive enrichment are shown. (C and F)
856 Sequence logos for the 6 bases surrounding the cleavage site for position -2:-1 (C) or -1:+1 (F).
857 Logos generated from the top 1% of either RNase L (215 sites) or EndoU-dependent cleavages
858 (306 sites). (G) UA cleavage scoring analysis. All UA sequences in the MHV genomic RNA with
859 ≥ 30 cyclic phosphate counts in either the UA[↓] or U[↓]A cleavage position were compared by
860 calculating the ratio of normalized counts (UA[↓] counts / U[↓]A counts). Ratios > 1 were scored as
861 UA[↓] (RNase L) sites and ratios < 1 were scored as U[↓]A sites (EndoU) and total number of
862 scored sites for either position are shown for each condition of viral infection in WT BMM at 9
863 and 12 hpi. (H) Model of EndoU and RNase L interaction at UA sites in MHV RNA.

864 **Figure 5. RNase L-dependent and EndoU-dependent cleavage sites in MHV RNA.**

865 (A) Schematic outline of analysis to identify EndoU/RNase L-dependent cyclic phosphate reads.
866 (B and C) Fold change values for the top 100 RNase L-dependent or EndoU-dependent
867 cleavage sites. Fold change in cyclic phosphate signal when comparing WT or IFNAR^(-/-) BMM
868 infected with MHV^(S), MHV^(V), PDE^{mut}, and EndoU^{mut} virus to RNase L^{-/-} BMM (B) or MHV^(S),
869 MHV^(V), PDE^{mut} virus to infection with EndoU^{mut} virus across all cell types (C) displayed as violin
870 scatter plot. Log2 fold change in the absence of RNase L activity (B) or in the absence of EndoU

871 activity (C) was calculated for each position in the MHV genomic RNA. Fold change values for
872 the top 100 RNase L-dependent or EndoU-dependent sites were compared in WT and IFNAR^{-/-}
873 BMM under conditions of infection with MHV^(S), MHV^(V), PDE^{mut}, and EndoU^{mut} virus at 12 hpi (B)
874 or in all cell types across conditions of infection with MHV^(S), MHV^(V), PDE^{mut} virus at 12 hpi.

875 (D) Frequency and location of RNase L-dependent cleavage sites in MHV RNA. Cyclic
876 phosphate counts at each position in the viral genome were normalized by removing signal that
877 occurred in the absence of RNase L, which emphasizes sites that are RNase L-dependent in
878 WT BMM infected with MHV^(S), and PDE^{mut} at 9 and 12 hpi. Labeled positions and dinucleotides
879 (-2 base : -1 base) on the graph of PDE^{mut} represent the top 15 RNase L-dependent cleavage
880 sites (B) with the greatest fold-change in RNase L activity (*site with robust cleavage without
881 canonical RNase L dinucleotide preference and independent of EndoU activity; not identified as
882 top site by RNase L fold change analysis).

883 (E) Frequency and location of EndoU-dependent cleavage sites in MHV RNA. Cyclic phosphate
884 counts at each position in the viral genome were normalized by removing signal that occurred in
885 the absence of EndoU, which emphasizes sites that are EndoU-dependent and RNase L-
886 independent in RNase L^{-/-} BMM infected with WT MHV^(V) at 9 and 12 hpi. Labeled positions and
887 dinucleotides (-1 base : +1 base) represent the top 15 EndoU-dependent cleavage sites with the
888 greatest fold-change in EndoU activity (C).

889 (F) Cumulative distribution of normalized counts by position of MHV genome for every position
890 with ≥ 10 cyclic phosphate counts across all cell types and infection conditions.

891 **Figure 6. Abundance of cyclic phosphate ends by MHV genomic region and MHV mRNA**
892 **abundance.** Sum of endonuclease cleavage sites in MHV RNA, by genomic regions: sum of
893 cyclic phosphate reads (A), sum of cyclic phosphate reads normalized by MHV mRNA
894 abundance (B) or sum of cyclic phosphate reads normalized by the length of the MHV genomic

895 region (C). (A) Sum of cyclic phosphate cDNA reads displayed by MHV RNA region for WT,
896 IFNAR^{-/-}, RNase L^{-/-} BMM across all conditions of viral infection at 12 hpi. Transcriptional
897 regulatory sequences (TRS) are numbered by their associated mRNA (2-7). Other MHV
898 genomic regions are labeled as shown in Figure 1A. (B) Frequency of endonuclease cleavage
899 sites in MHV RNA, by genomic regions, normalized by MHV mRNA abundance. Sum of cyclic
900 phosphate counts normalized by mRNA abundance at each capture base, displayed by MHV
901 genomic region for WT, IFNAR^{-/-}, RNase L^{-/-} BMM across all conditions of viral infection at 12
902 hpi. (C) Percent of sum of normalized counts per length of MHV genomic region for WT, IFNAR^{-/-}
903 ^{-/-} and RNase L^{-/-} BMM across all conditions of viral infection at 12 hpi. Dotted line represents
904 baseline percent of cleavage expected by cell type ([total number of cyclic phosphate counts /
905 total genome size x 100]). (D) Frequency and location of cleavage in the MHV TRS elements in
906 WT BMM during infection with MHV^(V) and EndoU^{mut} at 12 hpi. The x-axis includes the
907 sequence and position of the 6-base MHV TRS elements. (E) Normalized counts (sum of MHV
908 sg mRNA / sum of all MHV mRNAs) of MHV sg mRNAs detected in WT, IFNAR^{-/-}, RNase L^{-/-}
909 BMM across all conditions of viral infection at 9 and 12 hpi. (F) Sum of all MHV sg mRNAs
910 (RPM) for WT, IFNAR^{-/-}, RNase L^{-/-} BMM across all conditions of viral infection at 9 and 12 hpi.

911 **Figure 7. MHV secondary structures associated with RNase L-dependent and EndoU-**
912 **dependent cleavage sites.** (A and C) Nucleotide resolution graphs displaying normalized
913 counts by position for the regions encompassing secondary structure predictions. (B and D)
914 Secondary structures of frameshift stimulation element (B) and MHV 3'-UTR pseudoknot (D),
915 generated using available consensus alignment and the R-scape program (85). MHV A59
916 sequence mapped to consensus secondary structures using available covariation model and
917 the Infernal program (86). Base coloring of MHV A59 sequence based on normalized cDNA
918 reads as indicated in key for 12 hpi in WT BMM infected with MHV^(V). *Base RNase L-

919 dependent cleavage activity is increased in PDE^{mut} or EndoU^{mut} infection as compared to MHV^(V)
920 infection.

921 **Figure 8. Endoribonuclease cleavage of cellular RNAs and changes in host gene**

922 **expression.** RNase L-dependent cleavage sites in 18S rRNA (A & B). (A) RNase L-dependent

923 cleavage sites in 18S rRNA by fold change in signal when comparing WT or IFNAR^{-/-} BMM

924 mock-infected or infected with MHV^(S), MHV^(V), PDE^{mut}, and EndoU^{mut} virus to RNase L^{-/-} BMM.

925 Log₂ fold change in the absence of RNase L activity was calculated for each position in the

926 rRNA. The distribution of the top 100 RNase L-dependent cleavage sites were compared in WT

927 and IFNAR^{-/-} BMM under conditions of mock infection or infection with MHV^(S), MHV^(V), PDE^{mut},

928 and EndoU^{mut} virus at 9 hpi. 18S rRNA was cleaved in an RNase L-dependent manner at UU⁵⁴²,

929 UU⁵⁴³, UU⁷⁷¹ and UA⁷⁷². (B) RNase L-dependent cleavage of 18S rRNA at UU⁷⁷¹ and UA⁷⁷² at 9

930 and 12 hpi, predominantly in MHV PDE^{mut}- and EndoU^{mut}-infected WT BMM. (C) Volcano plot of

931 changes in host gene expression comparing MHV^(S)-infected and mock-infected WT BMM. Host

932 genes differentially expressed (FDR < 0.05) and upregulated (logFC > 2) or downregulated

933 (logFC < -2). (D) GO analysis: MHV EndoU^{mut} infection of WT BMM provokes increased

934 expression of host genes associated with exogenous dsRNA response. Categories of biological

935 processes with significantly upregulated genes (p < 0.01, log₂FC > 2) identified by comparing

936 MHV^(S)-infected and EndoU^{mut}-infected WT BMM to mock-infected WT BMM. Top 5 categories

937 significantly enriched (weightFisher < 0.01). (E) Expression of host genes in GO category

938 “response to exogenous dsRNA”. Expression (log₁₀ normalized counts) of genes in the GO

939 category “response to exogenous dsRNA” for WT BMM at 12 hpi: mock-infected (■) or MHV-

940 infected with MHV^(S) (●), MHV^(V) (▲), PDE^{mut} (+), and EndoU^{mut} (red-circle in black square). (F

941 and G) Differential host gene expression comparing mock-infected and MHV^(S)-infected cells at

942 12 hpi: WT BMM (F) and RNase L^{-/-} BMM (G). Upregulated (fold change > 2, FDR < 0.01) and

943 downregulated transcripts (fold change < -2, FDR < 0.01).

944 **Figure 9. EndoU targets in MHV RNA.** MHV RNA was targeted for cleavage by EndoU within
945 infected BMM. MHV RNA was cleaved by EndoU in all regions of the genome, at C[↓]A and U[↓]A
946 sequences. Because MHV RNA is a template for both viral mRNA translation and viral RNA
947 replication, cleavage by EndoU could inhibit both of these biosynthetic processes. Intriguingly,
948 MHV TRS sequences contain EndoU target sequences (C[↓]A and U[↓]A sequences). TRS6,
949 which was targeted more frequently by EndoU than other TRS elements, contains a C[↓]A target
950 sequence rather than a U[↓]A sequence. We postulate that EndoU cleaves MHV RNA in a
951 regulated manner, to inhibit negative-strand RNA synthesis, thereby inhibiting the accumulation
952 of viral dsRNA. Nsp16 (2' O-MT) could regulate EndoU-mediated cleavage of MHV RNA by
953 methylating C[↓]A and U[↓]A sequences. EndoU and RNase L cleave an overlapping set of UA
954 sequences within MHV, suggesting a functional interplay between host and viral
955 endoribonucleases.

956 SUPPLEMENTAL FIGURES AND TABLES

957 **Figure S1. Frequency and location of endoribonuclease cleavage sites in U6 snRNA and**
958 **MHV antigenomic RNA in WT, IFNAR^{-/-}, and RNase L^{-/-} BMM.** Normalized 2'-3'-cp cDNA
959 reads captured at each position along the (A) U6 snRNA and (B) MHV antigenomic RNA at 9
960 and 12 hpi with MHV^(S), MHV^(V), PDE^{mut}, and EndoU^{mut} virus in IFNAR^{-/-} BMM.

961 **Figure S2. Dinucleotide cleavage pattern in MHV genomic RNA downstream of captured**
962 **3' RNA end.** Percent total 2'-3'-cp cDNA reads captured at each dinucleotide in WT BMM at 9
963 and 12 hpi for bases +1:+2 and +2:+3 from the captured cleavage position (0-base).

964 **Figure S3. Endoribonuclease cleavage preferences in MHV RNA from IFNAR^{-/-} and RNase**
965 **L^{-/-} BMM.** (A) and (B) Dinucleotide specificity analysis for cleavage in MHV genomic RNA by
966 percent total cyclic phosphate cDNA reads captured at each 3'-dinucleotide at 9 and 12 hpi in
967 (A) IFNAR^{-/-} BMM for positions -2:-1 and in (B) RNase L^{-/-} BMM for positions -1:+1.

968 **Figure S4. Interaction between RNase L and EndoU cleavage at UA sequences in MHV**
969 **RNA.** (A) UA cleavage scoring analysis. All UA sequences in the MHV genomic RNA with ≥ 30
970 cyclic phosphate counts in either the UA \downarrow or U \downarrow A cleavage position were compared by
971 calculating the ratio of normalized counts (UA \downarrow counts / U \downarrow A counts). Ratios > 1 were scored as
972 UA \downarrow (RNase L) sites and ratios < 1 were scored as U \downarrow A sites (EndoU) and total number of
973 scored sites for either position are shown for each condition of viral infection in IFNAR^{-/-} and
974 RNase L^{-/-} BMM. (B) Frequency and location of UA positions in WT BMM under all conditions of
975 viral infection which had ≥ 50 counts at U \downarrow A positions and ≤ 1 counts at UA \downarrow positions. The top
976 5 of these positions by normalized count are labeled. (C) Frequency and location of UA
977 positions in IFNAR^{-/-} and RNase L^{-/-} BMM under all conditions of viral infection which had ≥ 50
978 counts at U \downarrow A positions and ≤ 1 counts at UA \downarrow positions.

979 **Figure S5. MHV RNA abundance and RNAseq reads across the MHV genome.** (A) Total
980 RNAseq normalized counts assigned to MHV genomic features for each library. (B) Coverage of
981 RNAseq read density across the MHV genome in reads per million.

982 **Figure S6. Frequency and location of endoribonuclease cleavage in MHV 3'-UTR.**
983 Nucleotide and sequence resolution graphs displaying normalized counts in (A) WT, (B) IFNAR⁻
984 ⁻ (C) RNase L⁻ BMM during infection with MHV^(V) and EndoU^{mut} MHV. Nucleotide resolution
985 graphs of region directly upstream of poly-A tail with cyclic phosphate counts normalized by
986 RNA abundance in (D) WT, (E) IFNAR⁻ (F) RNase L⁻ BMM.

987 **Figure S7. Regional cleavage of MHV RNA and total subgenomic mRNA abundance.** (A)
988 Sum of cyclic phosphate counts normalized by mRNA abundance displayed by region for WT,
989 IFNAR⁻, RNase L⁻ BMM across all conditions of viral infection at 12 hpi. (B) Percent of sum of
990 normalized counts per length of genomic region for WT, IFNAR⁻, RNase L⁻ BMM across all
991 conditions of viral infection at 12 hpi. Dotted line represents baseline percent of cleavage
992 expected by cell type ($[\text{total number of cyclic phosphate counts} / \text{total genome size} \times 100]$). (C)
993 Sum of all subgenomic mRNAs (RPM) for WT, IFNAR⁻, RNase L⁻ BMM across all conditions of
994 viral infection at 9 and 12 hpi.

995 **Figure S8. Cyclic phosphate sequencing analysis of experiment 2.** (A) Normalized cyclic
996 phosphate cDNA reads ($[\text{reads at each position} / \text{total reads in library}]$) aligning to host and viral
997 RNAs at 9 and 12 hpi in WT and RNase L⁻ bone marrow macrophages (BMM). (B) Putative
998 cleavage sites attributed to EndoU or RNase L were calculated from RNase L- or EndoU-
999 dependent signal generated by subtracting signal from each captured position that occurs in the
1000 absence of either enzyme (RNase L⁻ BMM or during EndoU^{mut} infection). These data were then
1001 filtered for sites with reads representing at least 0.01 % of total reads in the library. At each of
1002 these positions, the log₂ fold change in signal when either RNase L or EndoU were absent was
1003 calculated and sites with ≥ 2.5 fold change were called as putative RNase L or EndoU sites. (C)

1004 and D) Dinucleotide specificity analysis for cleavage in MHV genomic RNA by percent total
1005 cDNA reads captured at each 3'-dinucleotide in WT BMM at 9 and 12 hpi for (C) Dinucleotide
1006 analysis for positions -2: -1 and (D) Dinucleotide analysis for positions -1:+1 from captured
1007 cleavage position (0 position). (E) Cumulative distribution of normalized counts by position of
1008 the MHV genome for every position with ≥ 10 cyclic phosphates counts across all cell types
1009 and infection conditions. (F) UA cleavage scoring analysis. All UA sequences in the MHV
1010 genomic RNA with ≥ 30 cyclic phosphate counts in either the UA^ψ or U^ψA cleavage position
1011 were compared by calculating the ratio of normalized counts (UA^ψ counts / U^ψA counts). Ratios
1012 > 1 were scored as UA^ψ (RNase L) sites and ratios < 1 were scored as U^ψA sites (EndoU) and
1013 total number of scored sites for either position are shown for each condition of viral infection in
1014 WT BMM at 9 and 12 hpi. (H) Model of EndoU and RNase L interaction at UA sites in MHV RNA.
1015 (G) Nucleotide and sequence resolution graphs displaying normalized counts in WT BMM
1016 during infection with MHV^(S) and EndoU^{mut} MHV of region directly upstream of poly(A) tail.

1017 **Figure S9. Cyclic phosphate and RNAseq analysis of MHV RNA from experiment 2.** (A)
1018 Sum of normalized counts displayed by region for WT and RNase L^{-/-} BMM across all conditions
1019 of viral infection at 12 hpi. Transcription regulatory sequences (TRS) are numbered by their
1020 associated mRNA (2-7). Other genomic regions are labeled as shown in Figure 1A. (B) Sum of
1021 cyclic phosphate counts normalized by mRNA abundance and length of each genomic region
1022 $[(\text{sum per region (cyclic phosphate counts / RNAseq counts)} / \text{length of region (bp)} * 100) \text{ sum}$
1023 $\text{of cyclic phosphate abundance normalized counts per region}) / \text{length of region} * 100]$ displayed
1024 by region for WT and RNase L^{-/-} BMM across all conditions of viral infection at 12 hpi. (C)
1025 Normalized counts (sum of subgenomic mRNA / sum of all mRNAs) of subgenomic mRNAs
1026 detected in WT and RNase L^{-/-} BMM across all conditions of viral infection at 9 and 12 hpi. (D)
1027 Sum of all subgenomic mRNAs (RPM) for WT and RNase L^{-/-} BMM across all conditions of viral
1028 infection at 9 and 12 hpi.

1029 **Figure S10. RNase L targeting of rRNA and mRNA during WT and mutant MHV infection.**

1030 (A) Top 3 RNase L-dependent cleavage sites in 18S rRNA by fold change (\log_2 WT BMM /
1031 RNase L^{-/-} BMM) for all conditions of infection at 9 and 12 hpi in WT BMM. (B) Table of total
1032 RNase L- or EndoU-dependent cleavage sites in 18S, 28S, 5.8S, and 5S rRNA. RNase L- or
1033 EndoU-dependent cleavage were determined by identifying the top 1% of enzyme-dependent
1034 signal with a > 4 fold change in signal in the absence of RNase L or EndoU that match the
1035 RNase L ("UA", "UU", "UG", "UC") or EndoU ("UA", "CA") sequence preferences. (C)
1036 Distribution of sites in rRNA by fold change in signal when comparing WT or IFNAR^{-/-} BMM
1037 mock-infected or virus-infected with MHV^(S), MHV^(V), PDE^{mut}, and EndoU^{mut} virus to RNase L^{-/-}
1038 BMM. Log₂ fold change in the absence of RNase L activity was calculated for each position in
1039 the rRNA. The distribution of the top 100 RNase L-dependent sites were compared in WT and
1040 IFNAR^{-/-} BMM under conditions of mock infection or virus infection with MHV^(S), MHV^(V), PDE^{mut},
1041 and EndoU^{mut} virus at 12 hpi. (D) Distribution of sites in 18S, 28S, 5S, and 5.8S rRNA with the
1042 greatest fold change in signal when comparing mock infection or virus infection with MHV^(S),
1043 MHV^(V), PDE^{mut} virus to infection with EndoU^{mut} virus. Log₂ fold change in the absence of EndoU
1044 activity was calculated for each position in the rRNA. The distribution of the top 100 EndoU-
1045 dependent sites were compared in all cell types across conditions of mock infection or infection
1046 with MHV^(S), MHV^(V), PDE^{mut}, and EndoU^{mut} virus at 9 and 12 hpi.

1047 **Figure S11. Correlation between cyclic phosphate counts and RNA abundance.** (A and B).

1048 Correlation between mRNA abundance and 2'-3'-cp counts at each base captured in the MHV
1049 genome (all comparisons significant ($p < 10^{-50}$) for experiment 1 (A) and experiment 2 (B)). (C
1050 and D) Distribution of sites in MHV by normalized cyclic phosphates counts for sense and
1051 antisense RNAs from experiment 1 (C) and experiment 2 (D) across all conditions of infection
1052 and cell types. Positions are only shown if there was > 1 read in either the sense and antisense
1053 RNA.

1054 **Figure S12. Effect of WT and mutant MHV infection on other cellular endoribonucleases.**

1055 (A and B) Volcano plot of differentially expressed (FDR < 0.05) and upregulated (logFC > 2)/
1056 downregulated (logFC < -2) genes when comparing EndoU^{mut} infection to mock infection in WT
1057 BMM (A) or MHV^(s) infection to EndoU^{mut} infection in WT BMM. (C) Expression (log10
1058 normalized RNAseq counts) of RNase A, angiogenin, and RNaseT2 genes with at least 5 >
1059 normalized counts in all conditions.

1060 **Table S1 and S2. Dinucleotide enrichment and de-enrichment analysis at 9 and 12 hpi in**

1061 **WT BMM.** Complete tables of dinucleotide enrichment and de-enrichment for -2 base: +2 base
1062 (table 1) or -1 base:-1 base (table 2) from the captured RNA end (0-base position) for each
1063 condition of viral infection at 9 and 12 hpi in WT BMM by comparing the frequency of
1064 dinucleotide capture in experimental conditions to the frequency of occurrence for each
1065 dinucleotide in the MHV genomic RNA sequence (control). Significant enrichment was
1066 determined by adjusted p-value (q) for fold change (log₂(experiment / control)). (<0.02*,
1067 <0.0001**, <1×10⁸***).

1068 **Table S3: SNP variants in MHV genome related to endoribonuclease cleavage.** Table of all

1069 single nucleotide variants (SNPs) identify from alignments of RNAseq libraries to the MHV
1070 genome. The SNPs in **green** are sites where the mutation generated a “CA” dinucleotide that
1071 was cleaved by EndoU. The SNPs in **red** and **yellow** are the inactivating mutations in the
1072 EndoU and PDE domains of MHV respectively.

1073 **REFERENCES**

- 1074 1. **Ivanov KA, Hertzog T, Rozanov M, Bayer S, Thiel V, Gorbalenya AE, Ziebuhr**
1075 **J.** 2004. Major genetic marker of nidoviruses encodes a replicative
1076 endoribonuclease. *Proc Natl Acad Sci U S A* **101**:12694-12699.
- 1077 2. **Gorbalenya AE, Enjuanes L, Ziebuhr J, Snijder EJ.** 2006. Nidovirales:
1078 evolving the largest RNA virus genome. *Virus Res* **117**:17-37.
- 1079 3. **Wu A, Peng Y, Huang B, Ding X, Wang X, Niu P, Meng J, Zhu Z, Zhang Z,**
1080 **Wang J, Sheng J, Quan L, Xia Z, Tan W, Cheng G, Jiang T.** 2020. Genome
1081 Composition and Divergence of the Novel Coronavirus (2019-nCoV) Originating
1082 in China. *Cell Host Microbe* **27**:325-328.
- 1083 4. **Zhang M, Li X, Deng Z, Chen Z, Liu Y, Gao Y, Wu W, Chen Z.** 2017. Structural
1084 Biology of the Arterivirus nsp11 Endoribonucleases. *J Virol* **91**.
- 1085 5. **Zhang L, Li L, Yan L, Ming Z, Jia Z, Lou Z, Rao Z.** 2018. Structural and
1086 Biochemical Characterization of Endoribonuclease Nsp15 Encoded by Middle
1087 East Respiratory Syndrome Coronavirus. *J Virol* **92**.
- 1088 6. **Ricagno S, Egloff MP, Ulferts R, Coutard B, Nurizzo D, Campanacci V,**
1089 **Cambillau C, Ziebuhr J, Canard B.** 2006. Crystal structure and mechanistic
1090 determinants of SARS coronavirus nonstructural protein 15 define an
1091 endoribonuclease family. *Proc Natl Acad Sci U S A* **103**:11892-11897.

- 1092 7. **Bhardwaj K, Palaninathan S, Alcantara JM, Yi LL, Guarino L, Sacchettini JC,**
1093 **Kao CC.** 2008. Structural and functional analyses of the severe acute respiratory
1094 syndrome coronavirus endoribonuclease Nsp15. *J Biol Chem* **283**:3655-3664.
- 1095 8. **Nedialkova DD, Ulferts R, van den Born E, Lauber C, Gorbalenya AE,**
1096 **Ziebuhr J, Snijder EJ.** 2009. Biochemical characterization of arterivirus
1097 nonstructural protein 11 reveals the nidovirus-wide conservation of a replicative
1098 endoribonuclease. *J Virol* **83**:5671-5682.
- 1099 9. **Bredenbeek PJ, Pachuk CJ, Noten AF, Charite J, Luytjes W, Weiss SR,**
1100 **Spaan WJ.** 1990. The primary structure and expression of the second open
1101 reading frame of the polymerase gene of the coronavirus MHV-A59; a highly
1102 conserved polymerase is expressed by an efficient ribosomal frameshifting
1103 mechanism. *Nucleic Acids Res* **18**:1825-1832.
- 1104 10. **Sawicki SG, Sawicki DL, Siddell SG.** 2007. A contemporary view of
1105 coronavirus transcription. *J Virol* **81**:20-29.
- 1106 11. **Knoops K, Kikkert M, Worm SH, Zevenhoven-Dobbe JC, van der Meer Y,**
1107 **Koster AJ, Mommaas AM, Snijder EJ.** 2008. SARS-coronavirus replication is
1108 supported by a reticulovesicular network of modified endoplasmic reticulum.
1109 *PLoS Biol* **6**:e226.
- 1110 12. **van der Hoeven B, Oudshoorn D, Koster AJ, Snijder EJ, Kikkert M, Barcena**
1111 **M.** 2016. Biogenesis and architecture of arterivirus replication organelles. *Virus*
1112 *Res* **220**:70-90.

- 1113 13. **van Hemert MJ, van den Worm SH, Knoops K, Mommaas AM, Gorbalenya**
1114 **AE, Snijder EJ.** 2008. SARS-coronavirus replication/transcription complexes are
1115 membrane-protected and need a host factor for activity in vitro. PLoS Pathog
1116 **4:e1000054.**
- 1117 14. **Sawicki SG, Sawicki DL.** 1990. Coronavirus transcription: subgenomic mouse
1118 hepatitis virus replicative intermediates function in RNA synthesis. J Virol
1119 **64:1050-1056.**
- 1120 15. **Sethna PB, Hung SL, Brian DA.** 1989. Coronavirus subgenomic minus-strand
1121 RNAs and the potential for mRNA replicons. Proc Natl Acad Sci U S A **86:5626-**
1122 **5630.**
- 1123 16. **Sola I, Almazan F, Zuniga S, Enjuanes L.** 2015. Continuous and Discontinuous
1124 RNA Synthesis in Coronaviruses. Annu Rev Virol **2:265-288.**
- 1125 17. **Kazi L, Lissenberg A, Watson R, de Groot RJ, Weiss SR.** 2005. Expression of
1126 hemagglutinin esterase protein from recombinant mouse hepatitis virus
1127 enhances neurovirulence. J Virol **79:15064-15073.**
- 1128 18. **Lissenberg A, Vrolijk MM, van Vliet AL, Langereis MA, de Groot-Mijnes JD,**
1129 **Rottier PJ, de Groot RJ.** 2005. Luxury at a cost? Recombinant mouse hepatitis
1130 viruses expressing the accessory hemagglutinin esterase protein display reduced
1131 fitness in vitro. J Virol **79:15054-15063.**
- 1132 19. **Luytjes W, Bredenbeek PJ, Noten AF, Horzinek MC, Spaan WJ.** 1988.
1133 Sequence of mouse hepatitis virus A59 mRNA 2: indications for RNA

- 1134 recombination between coronaviruses and influenza C virus. *Virology* **166**:415-
1135 422.
- 1136 20. **Shieh CK, Lee HJ, Yokomori K, La Monica N, Makino S, Lai MM.** 1989.
1137 Identification of a new transcriptional initiation site and the corresponding
1138 functional gene 2b in the murine coronavirus RNA genome. *J Virol* **63**:3729-3736.
- 1139 21. **V'Kovski P, Gerber M, Kelly J, Pfaender S, Ebert N, Braga Lagache S,**
1140 **Simillion C, Portmann J, Stalder H, Gaschen V, Bruggmann R, Stoffel MH,**
1141 **Heller M, Dijkman R, Thiel V.** 2019. Determination of host proteins composing
1142 the microenvironment of coronavirus replicase complexes by proximity-labeling.
1143 *Elife* **8**.
- 1144 22. **Deng X, Hackbart M, Mettelman RC, O'Brien A, Mielech AM, Yi G, Kao CC,**
1145 **Baker SC.** 2017. Coronavirus nonstructural protein 15 mediates evasion of
1146 dsRNA sensors and limits apoptosis in macrophages. *Proc Natl Acad Sci U S A*
1147 **114**:E4251-E4260.
- 1148 23. **Kang H, Bhardwaj K, Li Y, Palaninathan S, Sacchettini J, Guarino L,**
1149 **Leibowitz JL, Kao CC.** 2007. Biochemical and genetic analyses of murine
1150 hepatitis virus Nsp15 endoribonuclease. *J Virol* **81**:13587-13597.
- 1151 24. **Ulferts R, Ziebuhr J.** 2011. Nidovirus ribonucleases: Structures and functions in
1152 viral replication. *RNA Biol* **8**:295-304.
- 1153 25. **Zust R, Cervantes-Barragan L, Habjan M, Maier R, Neuman BW, Ziebuhr J,**
1154 **Szretter KJ, Baker SC, Barchet W, Diamond MS, Siddell SG, Ludewig B,**

- 1155 **Thiel V.** 2011. Ribose 2'-O-methylation provides a molecular signature for the
1156 distinction of self and non-self mRNA dependent on the RNA sensor Mda5. *Nat*
1157 *Immunol* **12**:137-143.
- 1158 26. **Kindler E, Gil-Cruz C, Spanier J, Li Y, Wilhelm J, Rabouw HH, Zust R,**
1159 **Hwang M, V'Kovski P, Stalder H, Marti S, Habjan M, Cervantes-Barragan L,**
1160 **Elliot R, Karl N, Gaughan C, van Kuppeveld FJ, Silverman RH, Keller M,**
1161 **Ludewig B, Bergmann CC, Ziebuhr J, Weiss SR, Kalinke U, Thiel V.** 2017.
1162 Early endonuclease-mediated evasion of RNA sensing ensures efficient
1163 coronavirus replication. *PLoS Pathog* **13**:e1006195.
- 1164 27. **Deng X, van Geelen A, Buckley AC, O'Brien A, Pillatzki A, Lager KM,**
1165 **Faaberg KS, Baker SC.** 2019. Coronavirus Endoribonuclease Activity in Porcine
1166 Epidemic Diarrhea Virus Suppresses Type I and Type III Interferon Responses. *J*
1167 *Virology* **93**.
- 1168 28. **Zhao L, Birdwell LD, Wu A, Elliott R, Rose KM, Phillips JM, Li Y, Grinspan J,**
1169 **Silverman RH, Weiss SR.** 2013. Cell-type-specific activation of the
1170 oligoadenylate synthetase-RNase L pathway by a murine coronavirus. *J Virology*
1171 **87**:8408-8418.
- 1172 29. **Zhao L, Jha BK, Wu A, Elliott R, Ziebuhr J, Gorbalenya AE, Silverman RH,**
1173 **Weiss SR.** 2012. Antagonism of the interferon-induced OAS-RNase L pathway
1174 by murine coronavirus ns2 protein is required for virus replication and liver
1175 pathology. *Cell Host Microbe* **11**:607-616.

- 1176 30. **Zhao L, Rose KM, Elliott R, Van Rooijen N, Weiss SR.** 2011. Cell-type-specific
1177 type I interferon antagonism influences organ tropism of murine coronavirus. *J*
1178 *Virology* **85**:10058-10068.
- 1179 31. **Cooper DA, Banerjee S, Chakrabarti A, Garcia-Sastre A, Hesselberth JR,**
1180 **Silverman RH, Barton DJ.** 2015. RNase L targets distinct sites in influenza A
1181 virus RNAs. *J Virol* **89**:2764-2776.
- 1182 32. **Cooper DA, Jha BK, Silverman RH, Hesselberth JR, Barton DJ.** 2014.
1183 Ribonuclease L and metal-ion-independent endoribonuclease cleavage sites in
1184 host and viral RNAs. *Nucleic Acids Res* **42**:5202-5216.
- 1185 33. **Donovan J, Rath S, Kolet-Mandrikov D, Korennykh A.** 2017. Rapid RNase L-
1186 driven arrest of protein synthesis in the dsRNA response without degradation of
1187 translation machinery. *RNA* **23**:1660-1671.
- 1188 34. **Schutz K, Hesselberth JR, Fields S.** 2010. Capture and sequence analysis of
1189 RNAs with terminal 2',3'-cyclic phosphates. *RNA* **16**:621-631.
- 1190 35. **Coley SE, Lavi E, Sawicki SG, Fu L, Schelle B, Karl N, Siddell SG, Thiel V.**
1191 2005. Recombinant mouse hepatitis virus strain A59 from cloned, full-length
1192 cDNA replicates to high titers in vitro and is fully pathogenic in vivo. *J Virol*
1193 **79**:3097-3106.
- 1194 36. **Eriksson KK, Makia D, Thiel V.** 2008. Generation of recombinant coronaviruses
1195 using vaccinia virus as the cloning vector and stable cell lines containing
1196 coronaviral replicon RNAs. *Methods Mol Biol* **454**:237-254.

- 1197 37. **Thiel V, Herold J, Schelle B, Siddell SG.** 2001. Infectious RNA transcribed in
1198 vitro from a cDNA copy of the human coronavirus genome cloned in vaccinia
1199 virus. *J Gen Virol* **82**:1273-1281.
- 1200 38. **Roth-Cross JK, Stokes H, Chang G, Chua MM, Thiel V, Weiss SR,**
1201 **Gorbalenya AE, Siddell SG.** 2009. Organ-specific attenuation of murine
1202 hepatitis virus strain A59 by replacement of catalytic residues in the putative viral
1203 cyclic phosphodiesterase ns2. *J Virol* **83**:3743-3753.
- 1204 39. **Smith T, Heger A, Sudbery I.** 2017. UMI-tools: modeling sequencing errors in
1205 Unique Molecular Identifiers to improve quantification accuracy. *Genome Res*
1206 **27**:491-499.
- 1207 40. **Langmead B, Salzberg SL.** 2012. Fast gapped-read alignment with Bowtie 2.
1208 *Nat Methods* **9**:357-359.
- 1209 41. **Quinlan AR, Hall IM.** 2010. BEDTools: a flexible suite of utilities for comparing
1210 genomic features. *Bioinformatics* **26**:841-842.
- 1211 42. **Martin M.** 2011. Cutadapt removes adapter sequences from high-throughput
1212 sequencing reads. *EMBnetjournal* **17**:1-3.
- 1213 43. **Dobin A, Gingeras TR.** 2002. Mapping RNA-seq reads with STAR.29, 11.14.1-
1214 11.14.19. John Wiley & Sons, Inc.

- 1215 44. **Liao Y, Smyth GK, Shi W.** 2014. featureCounts: an efficient general purpose
1216 program for assigning sequence reads to genomic features. *Bioinformatics*
1217 **30**:923-930.
- 1218 45. **Love MI, Huber W, Anders S.** 2014. Moderated estimation of fold change and
1219 dispersion for RNA-seq data with DESeq2. *Genome Biol* **15**:550.
- 1220 46. **Patro R, Duggal G, Love MI, Irizarry RA, Kingsford C.** 2017. Salmon provides
1221 fast and bias-aware quantification of transcript expression. *Nat Methods* **14**:417-
1222 419.
- 1223 47. **Soneson C, Love MI, Robinson MD.** 2015. Differential analyses for RNA-seq:
1224 transcript-level estimates improve gene-level inferences. *F1000Res* **4**:1521.
- 1225 48. **Gu Z, Eils R, Schlesner M.** 2016. Complex heatmaps reveal patterns and
1226 correlations in multidimensional genomic data. *Bioinformatics* **32**:2847-2849.
- 1227 49. **Blighe K, Rana S, Lewis M.** 2019. EnhancedVolcano: Publication-ready volcano
1228 plots with enhanced colouring and labeling., R package version.
- 1229 50. **Alexa A, Rahnenfuhrer J.** 2019. topGO: Enrichment analysis for gene ontology.,
1230 R package version 2.37.0.
- 1231 51. **Bailey TL, Boden M, Buske FA, Frith M, Grant CE, Clementi L, Ren J, Li WW,**
1232 **Noble WS.** 2009. MEME SUITE: tools for motif discovery and searching. *Nucleic*
1233 *Acids Res* **37**:W202-208.

- 1234 52. **Wagih O.** 2017. ggseqlogo: a versatile R package for drawing sequence logos.
1235 Bioinformatics **33**:3645-3647.
- 1236 53. **Irigoyen N, Firth AE, Jones JD, Chung BY, Siddell SG, Brierley I.** 2016. High-
1237 Resolution Analysis of Coronavirus Gene Expression by RNA Sequencing and
1238 Ribosome Profiling. PLoS Pathog **12**:e1005473.
- 1239 54. **Riemyndy KA, Sheridan RM, Gillen A, Yu Y, Bennett CG, Hesselberth JR.**
1240 2017. valr: Reproducible genome interval analysis in R. F1000Res **6**:1025.
- 1241 55. **Li H.** 2011. A statistical framework for SNP calling, mutation discovery,
1242 association mapping and population genetical parameter estimation from
1243 sequencing data. Bioinformatics **27**:2987-2993.
- 1244 56. **Kivioja T, Vaharautio A, Karlsson K, Bonke M, Enge M, Linnarsson S,**
1245 **Taipale J.** 2011. Counting absolute numbers of molecules using unique
1246 molecular identifiers. Nat Methods **9**:72-74.
- 1247 57. **Mroczek S, Krwawicz J, Kutner J, Lazniewski M, Kucinski I, Ginalski K,**
1248 **Dziembowski A.** 2012. C16orf57, a gene mutated in poikiloderma with
1249 neutropenia, encodes a putative phosphodiesterase responsible for the U6
1250 snRNA 3' end modification. Genes Dev **26**:1911-1925.
- 1251 58. **Shchepachev V, Wischnewski H, Missiaglia E, Soneson C, Azzalin CM.** 2012.
1252 Mpn1, mutated in poikiloderma with neutropenia protein 1, is a conserved 3'-to-5'
1253 RNA exonuclease processing U6 small nuclear RNA. Cell Rep **2**:855-865.

- 1254 59. **Yang W.** 2011. Nucleases: diversity of structure, function and mechanism. *Q Rev*
1255 *Biophys* **44**:1-93.
- 1256 60. **Bhardwaj K, Sun J, Holzenburg A, Guarino LA, Kao CC.** 2006. RNA
1257 recognition and cleavage by the SARS coronavirus endoribonuclease. *J Mol Biol*
1258 **361**:243-256.
- 1259 61. **Harper JW, Fox EA, Shapiro R, Vallee BL.** 1990. Mutagenesis of residues
1260 flanking Lys-40 enhances the enzymatic activity and reduces the angiogenic
1261 potency of angiogenin. *Biochemistry* **29**:7297-7302.
- 1262 62. **Hofsteenge J, Moldow C, Vicentini AM, Zelenko O, Jarai-Kote Z, Neumann U.**
1263 1998. A single amino acid substitution changes ribonuclease 4 from a uridine-
1264 specific to a cytidine-specific enzyme. *Biochemistry* **37**:9250-9257.
- 1265 63. **Schwartz L, Cohen A, Thomas J, Spencer JD.** 2018. The Immunomodulatory
1266 and Antimicrobial Properties of the Vertebrate Ribonuclease A Superfamily.
1267 *Vaccines (Basel)* **6**.
- 1268 64. **Shapiro R, Vallee BL.** 1991. Interaction of human placental ribonuclease with
1269 placental ribonuclease inhibitor. *Biochemistry* **30**:2246-2255.
- 1270 65. **Birdwell LD, Zalinger ZB, Li Y, Wright PW, Elliott R, Rose KM, Silverman RH,**
1271 **Weiss SR.** 2016. Activation of RNase L by Murine Coronavirus in Myeloid Cells
1272 Is Dependent on Basal Oas Gene Expression and Independent of Virus-Induced
1273 Interferon. *J Virol* **90**:3160-3172.

- 1274 66. **Goebel SJ, Miller TB, Bennett CJ, Bernard KA, Masters PS.** 2007. A
1275 hypervariable region within the 3' cis-acting element of the murine coronavirus
1276 genome is nonessential for RNA synthesis but affects pathogenesis. *J Virol*
1277 **81**:1274-1287.
- 1278 67. **Peng YH, Lin CH, Lin CN, Lo CY, Tsai TL, Wu HY.** 2016. Characterization of
1279 the Role of Hexamer AGUAAA and Poly(A) Tail in Coronavirus Polyadenylation.
1280 *PLoS One* **11**:e0165077.
- 1281 68. **Zust R, Miller TB, Goebel SJ, Thiel V, Masters PS.** 2008. Genetic interactions
1282 between an essential 3' cis-acting RNA pseudoknot, replicase gene products,
1283 and the extreme 3' end of the mouse coronavirus genome. *J Virol* **82**:1214-1228.
- 1284 69. **Volk A, Hackbart M, Deng X, Cruz-Pulido Y, O'Brien A, Baker SC.** 2020.
1285 Coronavirus Endoribonuclease and Deubiquitinating Interferon Antagonists
1286 Differentially Modulate the Host Response during Replication in Macrophages. *J*
1287 *Virol* doi:10.1128/JVI.00178-20.
- 1288 70. **Greulich W, Wagner M, Gaidt MM, Stafford C, Cheng Y, Linder A, Carell T,**
1289 **Hornung V.** 2019. TLR8 Is a Sensor of RNase T2 Degradation Products. *Cell*
1290 **179**:1264-1275 e1213.
- 1291 71. **Dyer KD, Rosenberg HF.** 2005. The mouse RNase 4 and RNase 5/ang 1 locus
1292 utilizes dual promoters for tissue-specific expression. *Nucleic Acids Res*
1293 **33**:1077-1086.

- 1294 72. **Deng X, Baker SC.** 2018. An "Old" protein with a new story: Coronavirus
1295 endoribonuclease is important for evading host antiviral defenses. *Virology*
1296 **517**:157-163.
- 1297 73. **Hackbart M, Deng X, Baker SC.** 2020. Coronavirus endoribonuclease targets
1298 viral polyuridine sequences to evade activating host sensors. *Proc Natl Acad Sci*
1299 *U S A* **117**:8094-8103.
- 1300 74. **Sawicki SG, Sawicki DL.** 1986. Coronavirus minus-strand RNA synthesis and
1301 effect of cycloheximide on coronavirus RNA synthesis. *J Virol* **57**:328-334.
- 1302 75. **Kirchdoerfer RN, Ward AB.** 2019. Structure of the SARS-CoV nsp12
1303 polymerase bound to nsp7 and nsp8 co-factors. *Nat Commun* **10**:2342.
- 1304 76. **te Velthuis AJ, Arnold JJ, Cameron CE, van den Worm SH, Snijder EJ.** 2010.
1305 The RNA polymerase activity of SARS-coronavirus nsp12 is primer dependent.
1306 *Nucleic Acids Res* **38**:203-214.
- 1307 77. **Imbert I, Guillemot JC, Bourhis JM, Bussetta C, Coutard B, Egloff MP,**
1308 **Ferron F, Gorbalenya AE, Canard B.** 2006. A second, non-canonical RNA-
1309 dependent RNA polymerase in SARS coronavirus. *EMBO J* **25**:4933-4942.
- 1310 78. **Menachery VD, Yount BL, Jr., Josset L, Gralinski LE, Scobey T,**
1311 **Agnihothram S, Katze MG, Baric RS.** 2014. Attenuation and restoration of
1312 severe acute respiratory syndrome coronavirus mutant lacking 2'-o-
1313 methyltransferase activity. *J Virol* **88**:4251-4264.

- 1314 79. **Daffis S, Szretter KJ, Schriewer J, Li J, Youn S, Errett J, Lin TY, Schneller S,**
1315 **Zust R, Dong H, Thiel V, Sen GC, Fensterl V, Klimstra WB, Pierson TC,**
1316 **Buller RM, Gale M, Jr., Shi PY, Diamond MS.** 2010. 2'-O methylation of the
1317 viral mRNA cap evades host restriction by IFIT family members. *Nature* **468**:452-
1318 456.
- 1319 80. **Dong H, Chang DC, Hua MH, Lim SP, Chionh YH, Hia F, Lee YH, Kukkaro P,**
1320 **Lok SM, Dedon PC, Shi PY.** 2012. 2'-O methylation of internal adenosine by
1321 flavivirus NS5 methyltransferase. *PLoS Pathog* **8**:e1002642.
- 1322 81. **Ray D, Shah A, Tilgner M, Guo Y, Zhao Y, Dong H, Deas TS, Zhou Y, Li H,**
1323 **Shi PY.** 2006. West Nile virus 5'-cap structure is formed by sequential guanine
1324 N-7 and ribose 2'-O methylations by nonstructural protein 5. *J Virol* **80**:8362-8370.
- 1325 82. **Szretter KJ, Daniels BP, Cho H, Gainey MD, Yokoyama WM, Gale M, Jr.,**
1326 **Virgin HW, Klein RS, Sen GC, Diamond MS.** 2012. 2'-O methylation of the viral
1327 mRNA cap by West Nile virus evades ifit1-dependent and -independent
1328 mechanisms of host restriction in vivo. *PLoS Pathog* **8**:e1002698.
- 1329 83. **Burke JM, Moon SL, Matheny T, Parker R.** 2019. RNase L Reprograms
1330 Translation by Widespread mRNA Turnover Escaped by Antiviral mRNAs. *Mol*
1331 *Cell* **75**:1203-1217 e1205.
- 1332 84. **Rath S, Prangle E, Donovan J, Demarest K, Wingreen NS, Meir Y,**
1333 **Korenykh A.** 2019. Concerted 2-5A-Mediated mRNA Decay and Transcription

- 1334 Reprogram Protein Synthesis in the dsRNA Response. *Mol Cell* **75**:1218-1228
1335 e1216.
- 1336 85. **Rivas E, Clements J, Eddy SR.** 2017. A statistical test for conserved RNA
1337 structure shows lack of evidence for structure in lncRNAs. *Nat Methods* **14**:45-48.
- 1338 86. **Nawrocki EP, Eddy SR.** 2013. Infernal 1.1: 100-fold faster RNA homology
1339 searches. *Bioinformatics* **29**:2933-2935.
- 1340

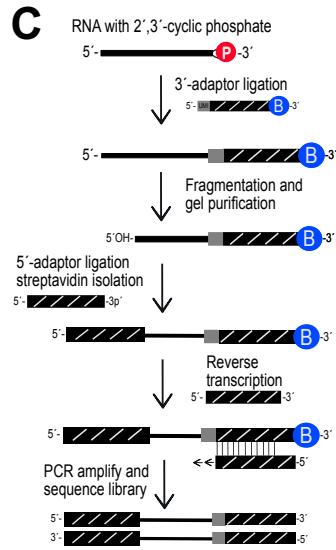
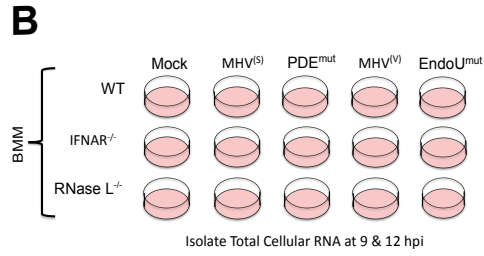
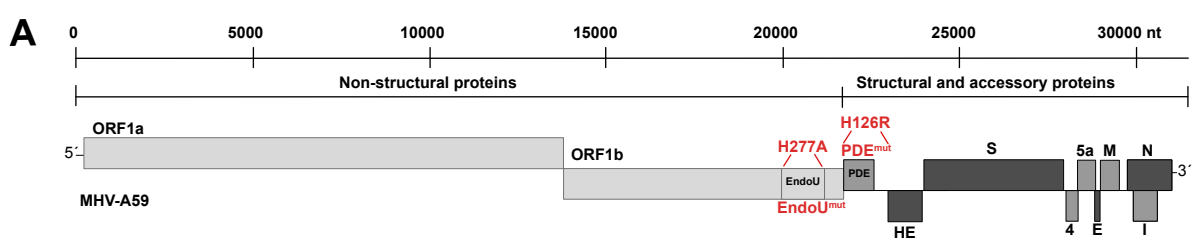


Figure 1

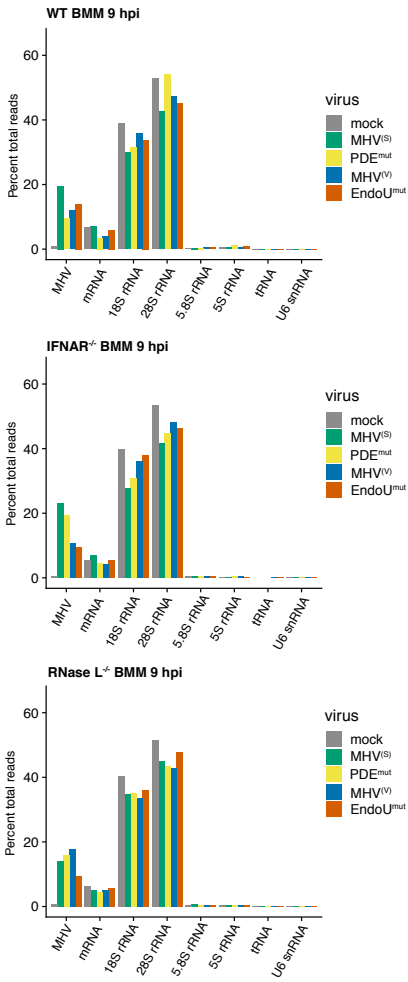
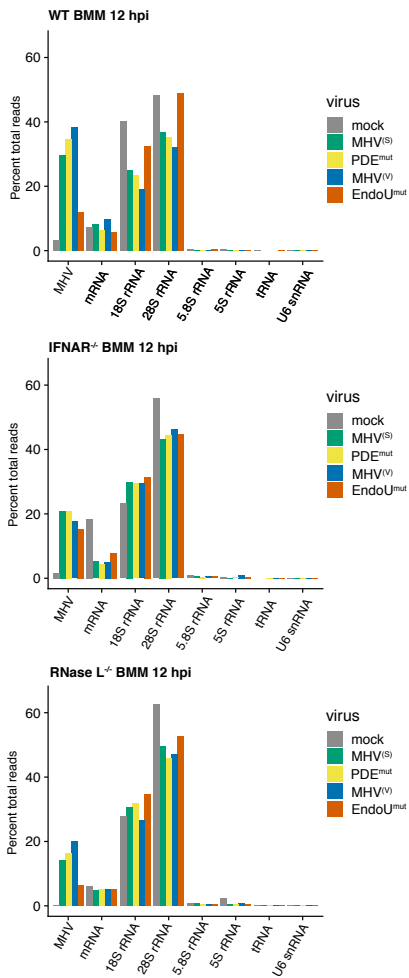
A**B**

Figure 2

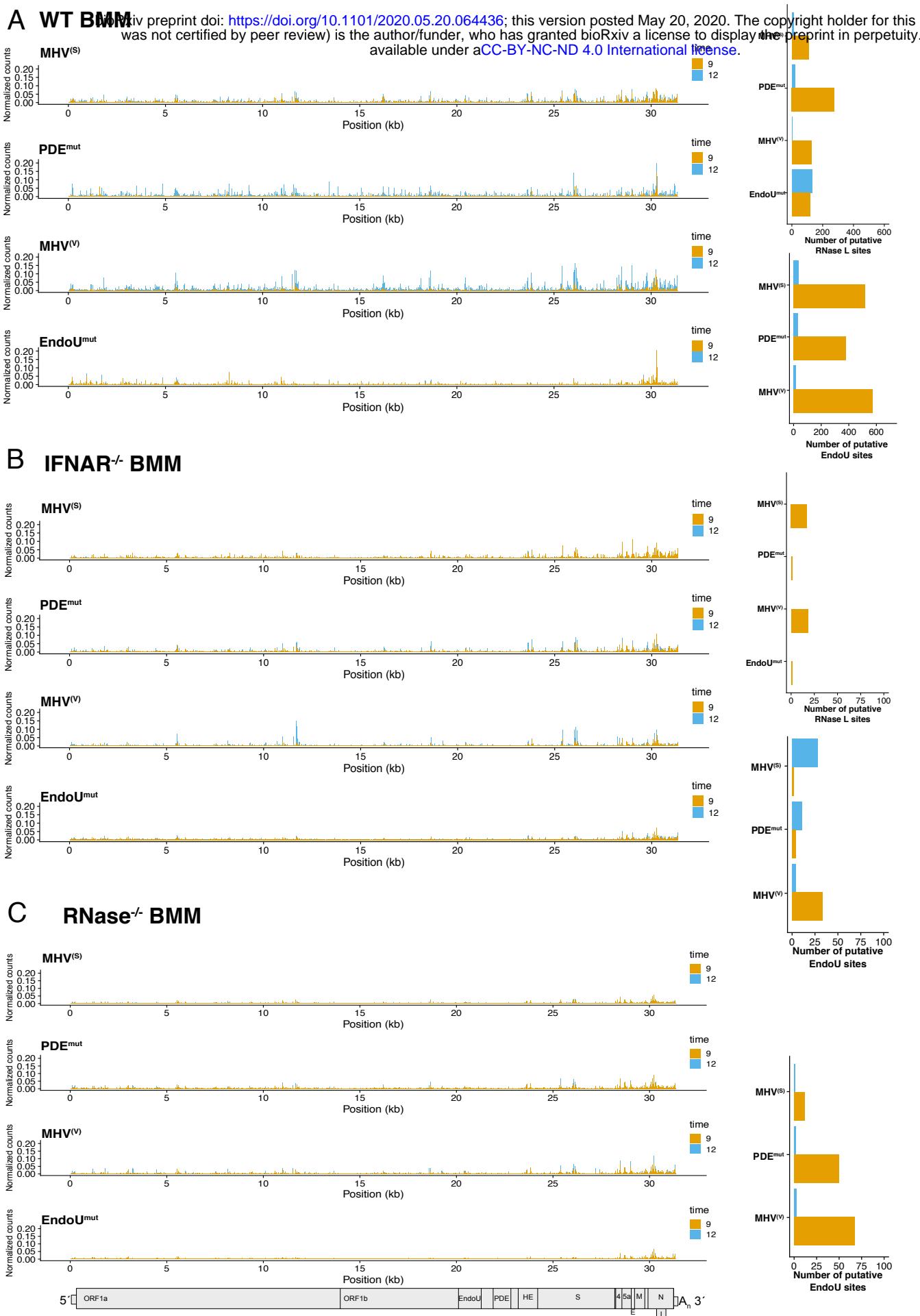
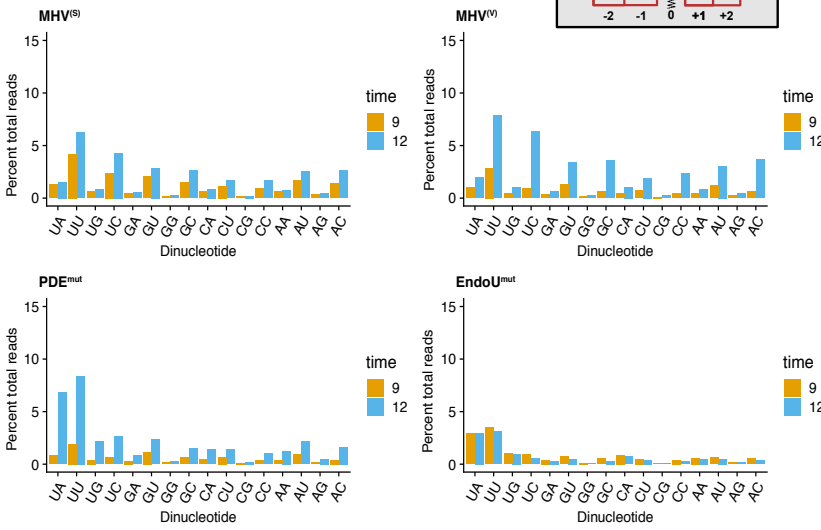


Figure 3

Dinucleotide cleavage analysis

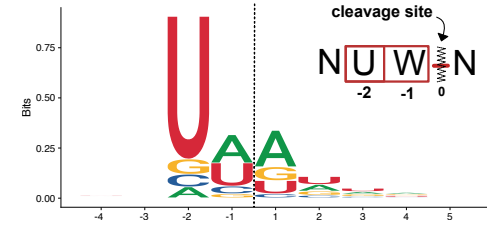
A Position -2 to -1 dinucleotide analysis



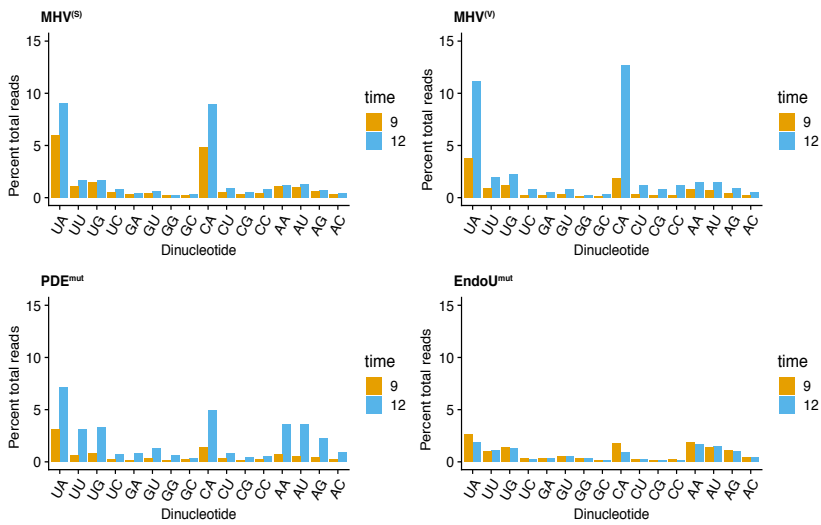
B Dinucleotide enrichment in WT BMM (position -2 to -1)

Dinucleotide	MHV ^(S) Fold change	MHV ^(V) Fold change	PDE ^{mut} Fold change	EndoU ^{mut} Fold change
UA	-0.57	-0.59	1.36***	1.71***
UU	1.01***	0.97***	1.22***	1.35***
UC	1.80***	1.99***	0.87***	0.15**
GU	0.29***	0.15**	-0.23	-0.94
GC	0.69***	0.78***	-0.30	-1.01
CA	-0.89	-1.00	-0.42	0.20**
CC	0.52**	0.62**	-0.45	-1.03
AU	0.10*	0.00	-0.34	-0.90
AC	0.98***	1.11***	0.10*	-0.61

C RNase L cleavage preference



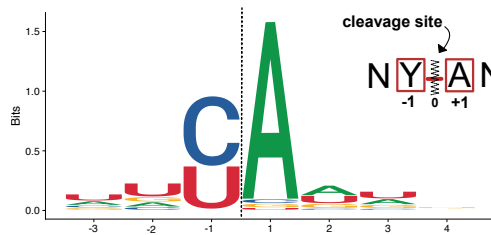
D Position -1 to +1 dinucleotide analysis



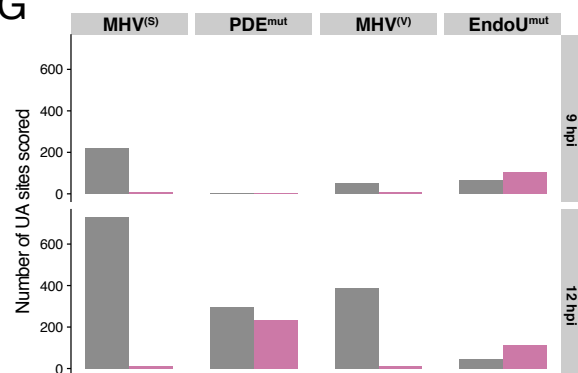
E Dinucleotide enrichment in WT BMM (position -1 to +1)

Dinucleotide	MHV ^(S) Fold change	MHV ^(V) Fold change	PDE ^{mut} Fold change	EndoU ^{mut} Fold change
UA	2.00***	1.93***	1.43***	1.02***
UG	-0.82	-0.79	-0.06	0.15**
CA	2.46***	2.60***	1.40***	0.56***
AA	-0.83	-0.89	0.51**	0.98***
AU	-0.88	-1.00	0.37***	0.62***
AG	-1.36	-1.44	0.04	0.41***

F EndoU cleavage preference



G



H

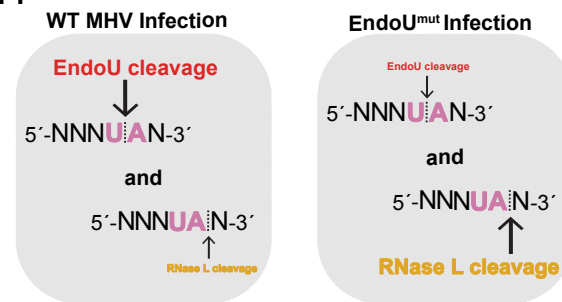


Figure 4

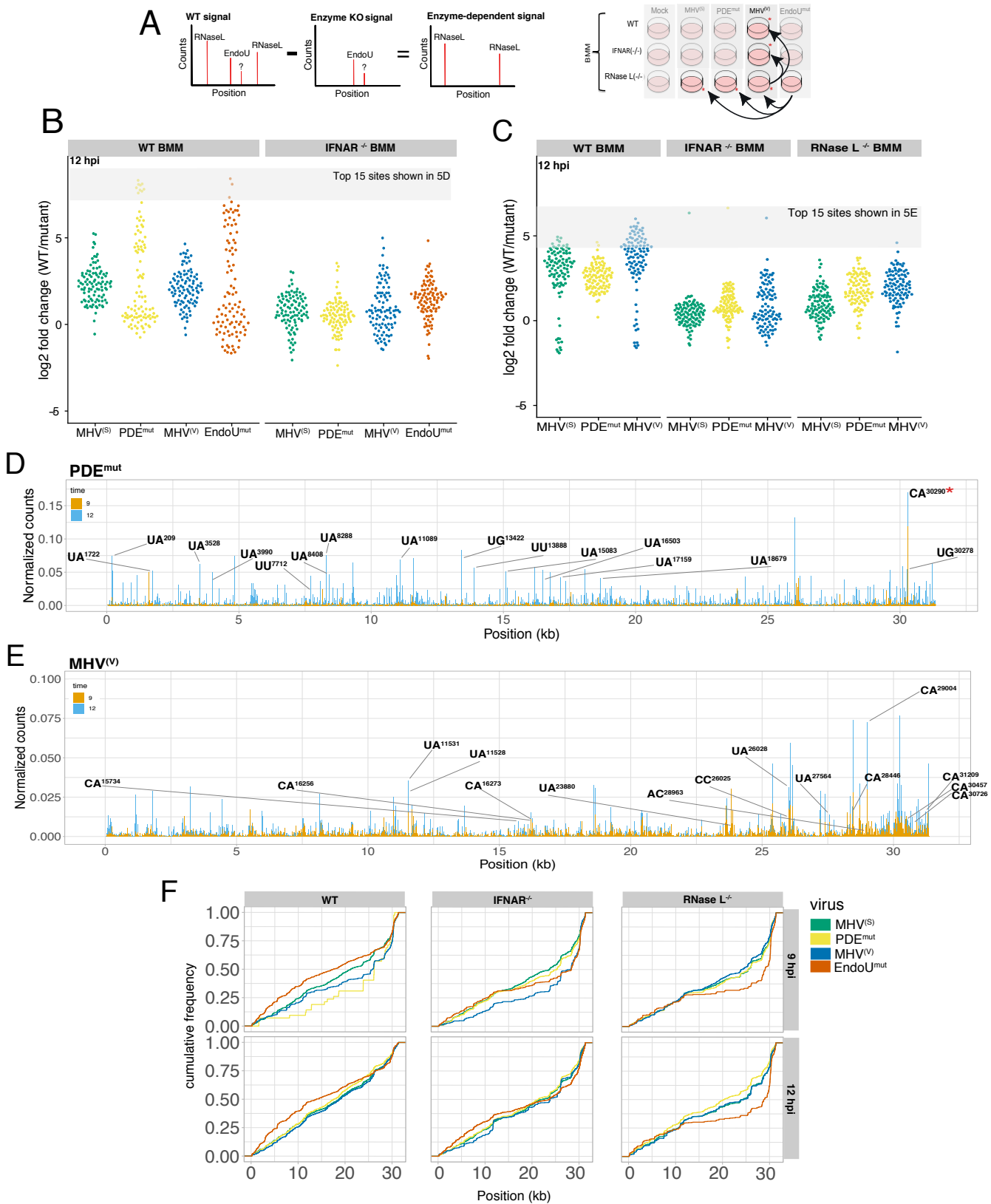


Figure 5

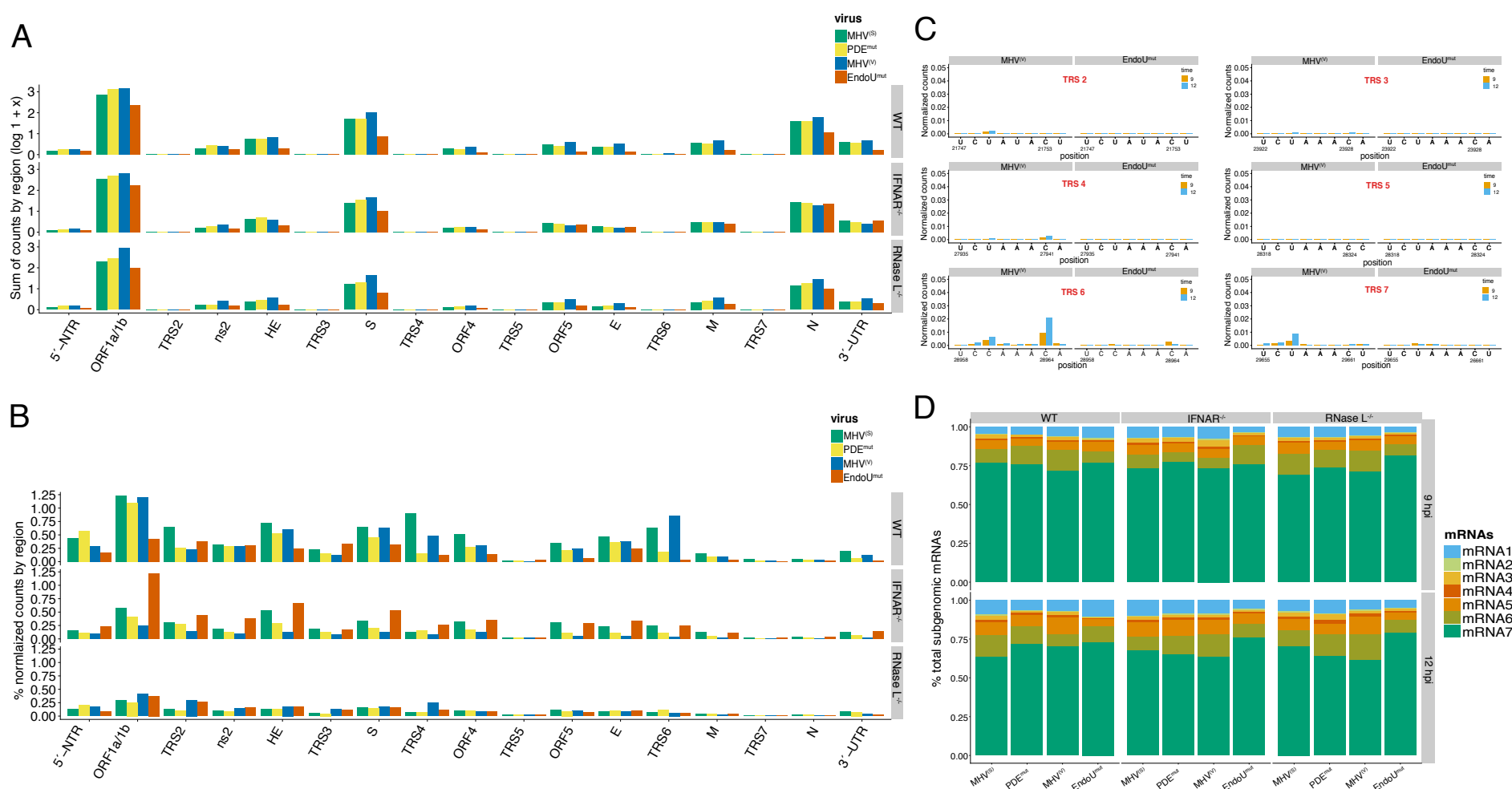
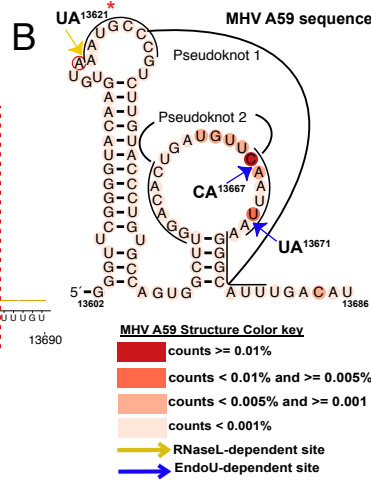
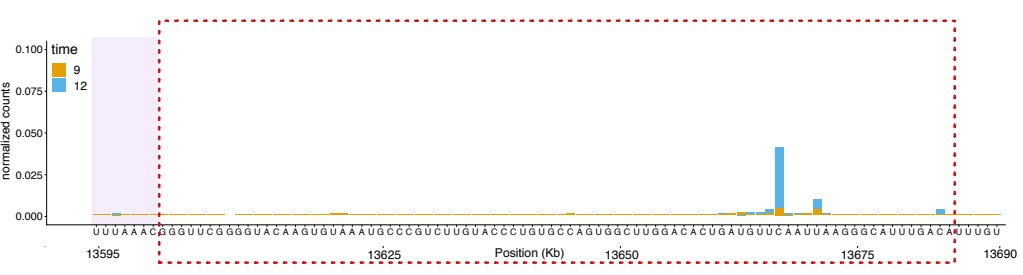


Figure 6

A Frameshift stimulation element for ORF1



C Pseudoknot in 3'-UTR

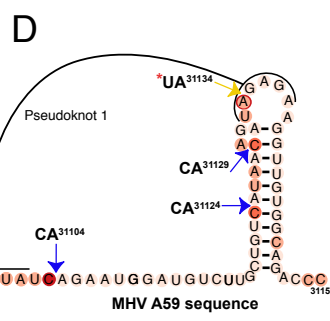
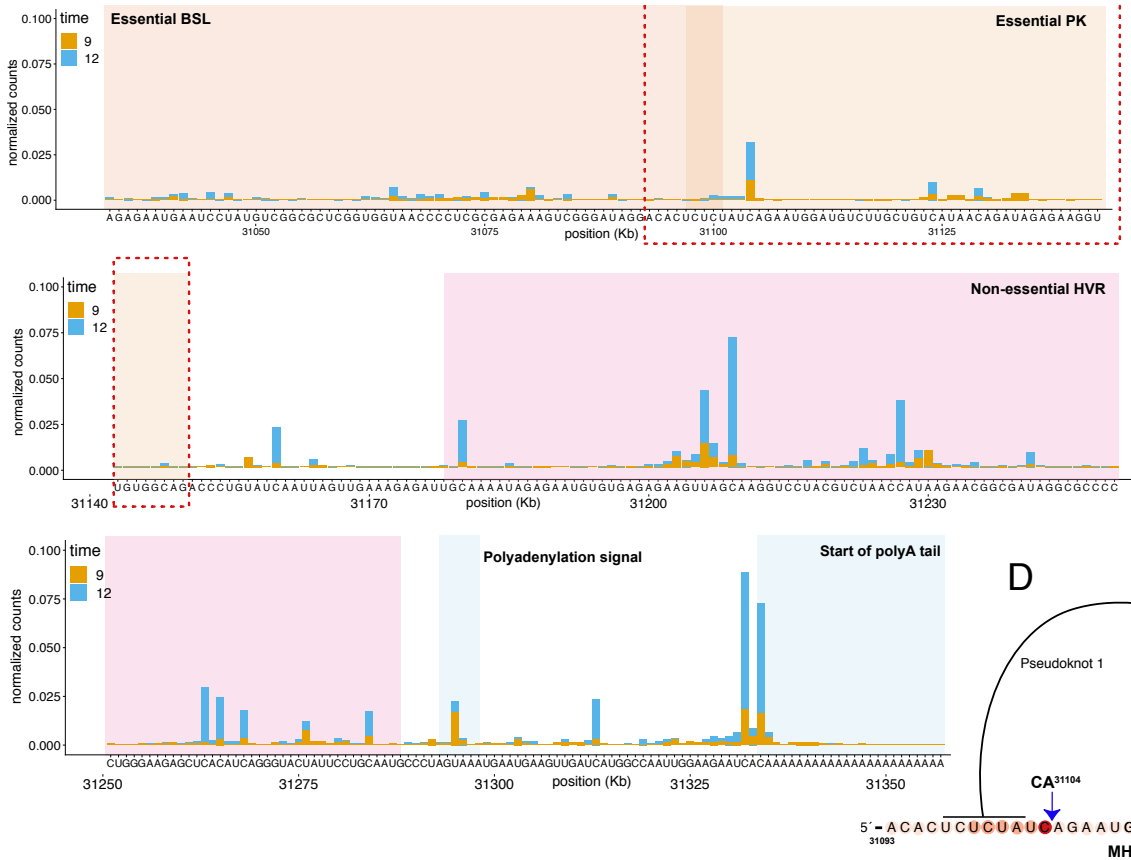


Figure 7

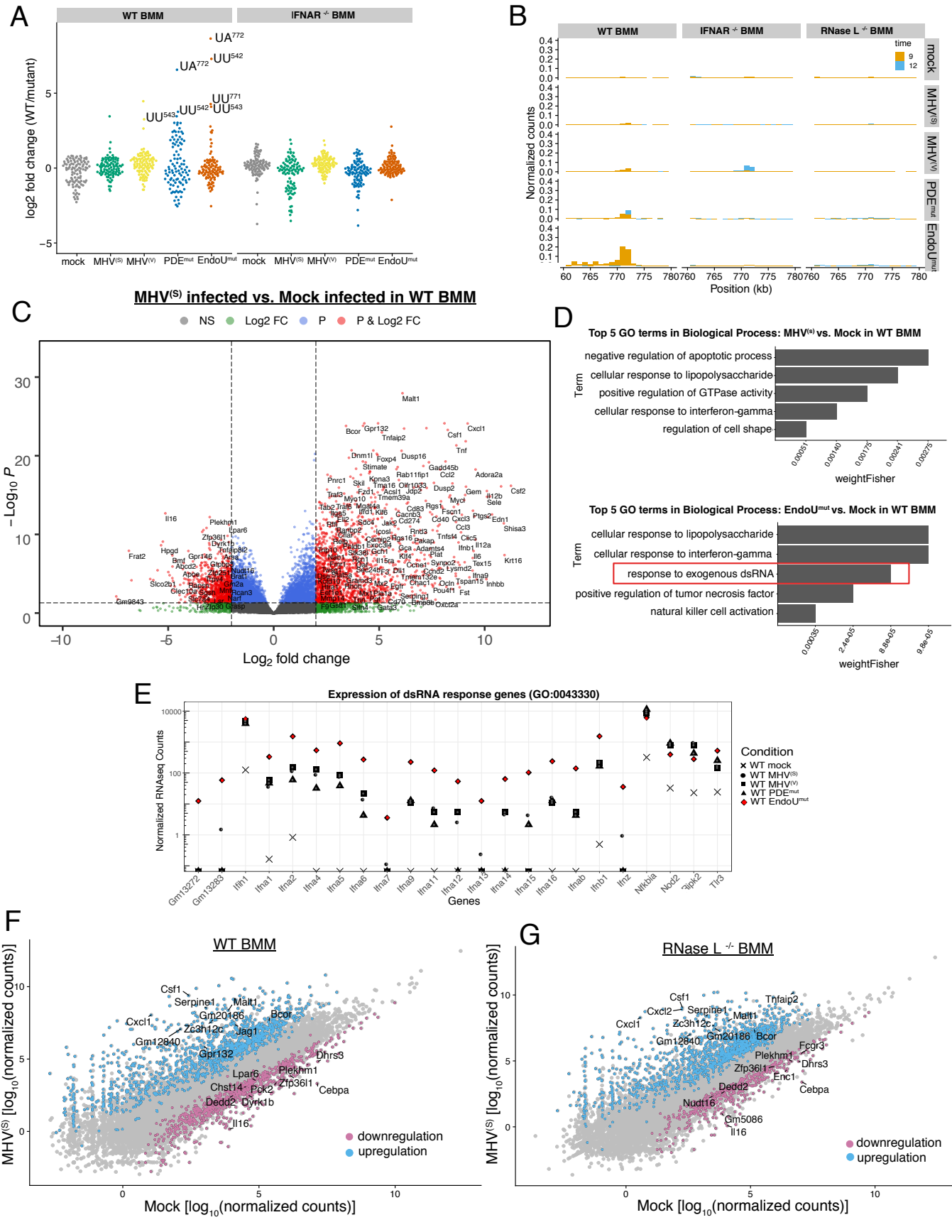


Figure 8

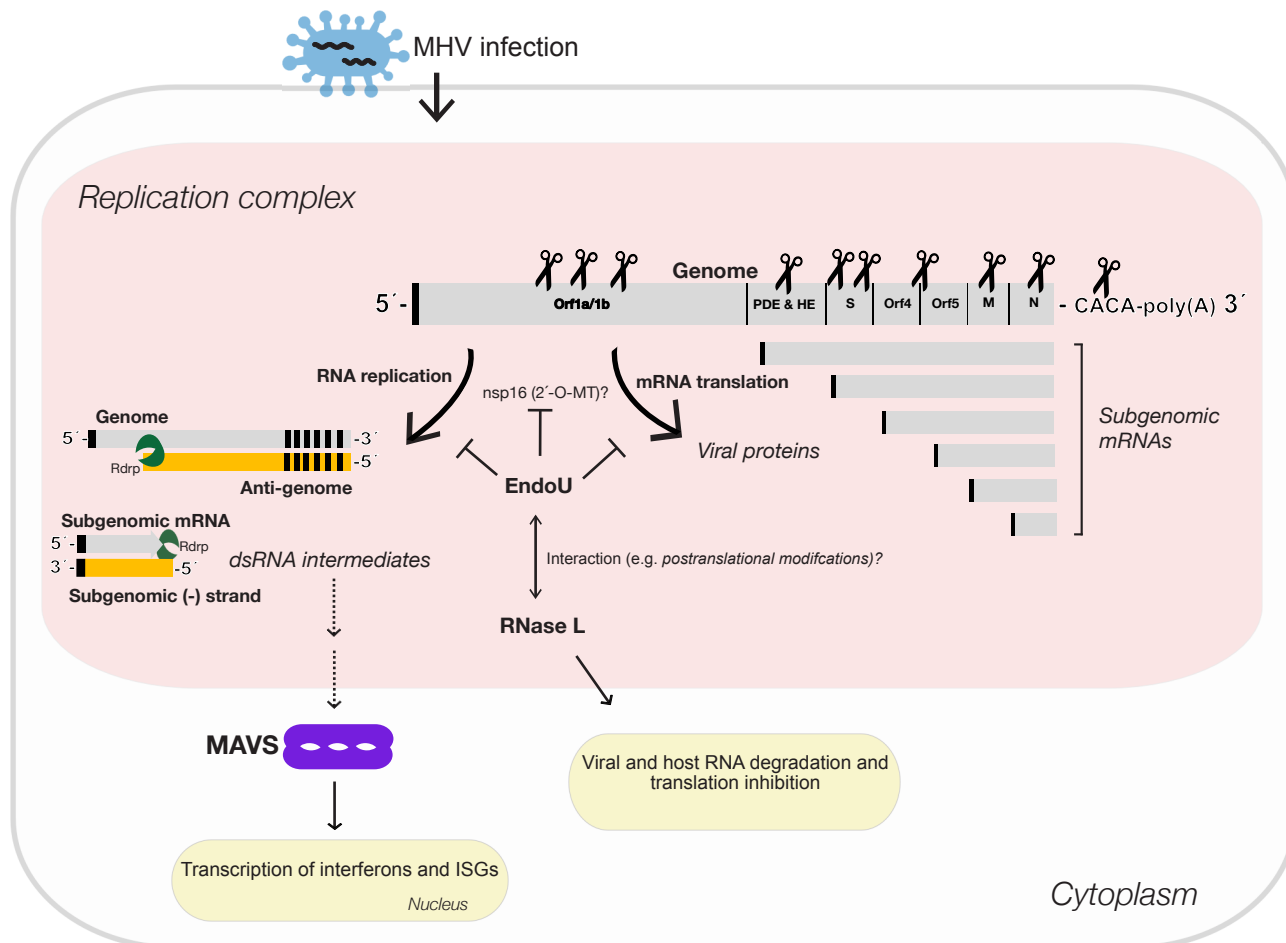


Figure 9